ABSTRACT

Title of Thesis: **MICRORESONATORS AND PHOTONIC CRYSTALS FOR QUANTUM OPTICS AND SENSING**

Sina Sahand, Master of Science, 2008

Thesis Directed By: **Professor Edo Waks**
Department of Electrical Engineering

The ability to store and manipulate light on micro-to-nanometer scales opens up doors of opportunity in biological sensing, quantum information, and creating all-optical interconnects on a chip. In this thesis, we present our effort along these directions. We take advantage of silicon nitride photonic crystals and microdisk resonators to confine and manipulate photons in the visible spectrum. We present a novel cavity design to obtain high quality-factor cavities and present our fabrication process. In addition, we present a novel techniques aimed at coupling cadmium-selenide colloidal QDs to photonic crystal cavities and discuss a method for freezing their kinetics through solidifying the liquid. This technique takes advantage of electroosmotic flow in microfluidic channels to control and steer QDs. Moreover, we analyze theoretically some interesting phenomenon, such as, coupling two quantum dots to a cavity.

MICRORESONATORS AND PHOTONIC CRYSTALS FOR QUANTUM OPTICS AND SENSING

by

Sina Sahand

Thesis submitted to the Faculty of the Graduate School of the
University of Maryland, College Park, in partial fulfillment
of the requirements for the degree of
Master of Science
2008

Advisory Committee:
Assistant Professor Edo Waks
Professor Christopher Davis
Associate Professor Thomas E. Murphy

ACKNOWLEDGEMENTS

This thesis would not have been possible without the help and contributions of my colleagues, friends, and family. First and foremost, I would like to acknowledge my advisor, Prof. Edo Waks for giving me the opportunity to work on these challenging and interesting projects. Dr. Waks had just joined the faculty staff at the University of Maryland when I met him. His ambition and novel ideas, together with an extraordinary good character had a great impact on me. I was fortunate to be one of his first students to go through the phase of project development and to work through different ideas and projects. Dr. Waks has always been very supportive and has always made himself available for help and advice. With great energy and enthusiasm, he has helped me to get through the set backs and the challenges of research. It has been a great pleasure to work with and learn from such an extraordinary individual. I would also like to thank some of the graduate students Roland Probst, Chad Ropp, and Deepak Sridharan, who I worked with as a team. Special gratitude to Prof. Christopher Davis and Prof. Thomas E. Murphy for sparing their invaluable time reading this manuscript and being on my thesis committee; they are amongst the finest educators that I have learned from during my academic career. I would also like to thank the University of Maryland clean-room staff for their help and training. Last but not least, I am grateful to my family who stood by me, cared for me, and continuously supported me throughout my whole life, particularly throughout these years. They are my primary teachers who gave me the passion for education in order to better serve society.

DEDICATION

I dedicate this thesis to Niloofar, for being an inspiration until the very end. You will be forever missed.

TABLE OF CONTENTS

LIST OF FIGURES

CHAPTER 1

CHAPTER 2

CHAPTER 5

CHAPTER 6

Appendix A

CHAPTER 1: Introduction

Physical constraints in further miniaturizing silicon-based devices to follow up with Moore's law, processing information with the speed of light, and optical sensing have been some of the motivations in developing integrated photonics on a chip. For this reason, creating a mechanism for storing, guiding, and manipulating light is crucial. Optical cavities best achieve this purpose by providing unprecedented interaction of light with matter. Group III-V provide the most popular materials used for this purpose, where there is a very high index-contrast. However, these materials operate in the infrared region of the spectrum and are toxic. Therefore, we investigate silicon nitride optical cavities with the advantages of operating in the visible spectrum, their low cost, bio-compatibility, and their monolithic integration with CMOS technology.

Storage of quantum information is most easily done in single atomic systems. The semiconductor analogy to an atomic system is a quantum dot (QD), a three dimensionally confined quantum structure. QDs have the advantage that they posses very large oscillator strengths, and can be easily localized without the use of atomic traps. In this letter, we report steering of CdSe colloidal QDs in microfluidic channels, placed on top of a membrane of photonic crystal cavities. The idea is to steer a QD on the surface of a cavity and to freeze its kinetics through changing the chemical properties of the liquid, once a resonant match is found. Implementing this idea promises the construction of optical interconnects on a chip, where cavities are connected through optical waveguides. Interaction between cavities is facilitated though reflecting weak coherent light, known as Dipole Induced Transparency [1]. This scheme has the advantage to controllably couple a quantum dot to a cavity when compared to present techniques, where an array of

cavities is constructed and quantum dots are grown (or formed) randomly with the promise of finding a cavity that is on resonance with the QD.

We break up this thesis as follows: in the remaining part of this chapter we will briefly discuss DIT and colloidal QDs. In chapter 2, we will discuss the theory and simulation of photonic crystal cavities, and we present microdisks resonators in chapter 3. In chapter 4, we present our effort in steering QDs in microfluidic channels placed on a membrane of silicon nitride. In chapter 5, we derive a formulism for calculating energy transfer and its efficiency when two QDs with different sizes are coupled to an optical cavity. Later, in chapter 6, we present our efforts towards fabricating photonic crystal cavities, microdisk resonators, silicon nitride membranes, and green semiconductor lasers. We finally conclude this thesis and point out some future directions in chapter 7.

1. 1 Dipole Induced Transparency

To store quantum information, two stable states (|0> and |1>) are needed. Moreover, it is vital to realize a method for implementing interactions between qubits. Recently, a new method for achieving these interactions, called Dipole Induced Transparency (DIT), has been proposed. In this method, quantum information is stored in QDs coupled to optical micro-cavities. The micro-cavities are interconnected by waveguides that serve as optical interconnects. Interactions are created by reflecting weak coherent light from the cavities. This implementation has the advantage that it eliminates the need for selectively coupling and decoupling qubits, which is achieved by routing a weak coherent light. Taking advantage of DIT, QD entanglement [2] and Bell Measurement [1], which are the foundations for quantum-computing, have been proposed. Figure 1.1 shows the schematic for a quantum dot coupled to a double sided cavity-waveguide structure,

presented in [1]. Figure 1.2 a and b, compares the transmission and reflection coefficients of light entering the input of the waveguide without and with the QD coupled to the cavity.

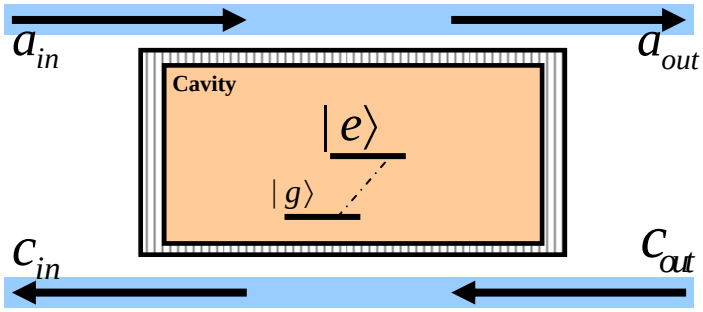

***Figure 1.1**: Quantum dot coupled to a double sided cavity-waveguide structure.*

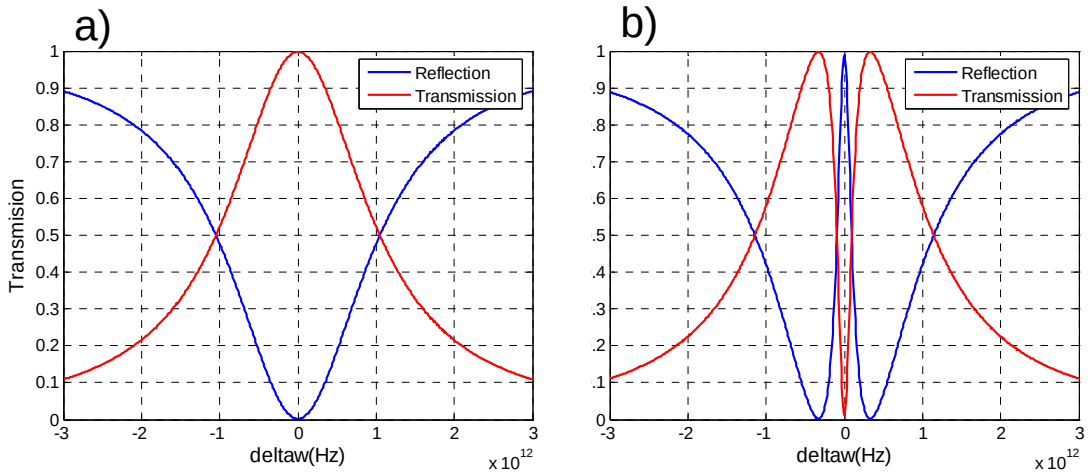

***Figure 1.2**: a) Transmission and reflection of light into the waveguide without the quantum dot (QD is not coupled to the cavity). b) Transmission and reflection when quantum dot is coupled to the cavity*

Therefore, the QD in the cavity acts as an optical switch as its state (coupling) controls the reflection or transmission of light in the waveguide.

1.2 Quantum Dots (QDs)

Colloidal QDs are inorganic particles that are typically a few nanometers in size. Fluorescence emission spectrum of these dots is very bright, and their linewidth is very

narrow. These particles could be tuned to different wavelengths by engineering their size through the growth process. Moreover, they are very stable against photobleaching and have a very broad absorption spectrum. In addition, colloidal QDs are more attractive in comparison to other semiconductor nanocrystals for the applications of enhancement and inhabitation of spontaneous emission when coupled to an optical cavity, such as a photonic crystal or a microdisk resonator, for the following reasons: First, quantum dots can be diluted to lower concentrations, and thus achieving the coupling of a single QD to the cavity is possible. Second, colloidal QDs can be functionalized differently by adding a capping layer and their application is not limited to a specific set of materials. Colloidal qds have been widely investigated for applications in DNA tagging and protein conformation.

Our first exposure to quantum dots was with Lead Sulfide (PbS) nanocrystals with emission wavelength of about 1μm, which were analyzed for coupling to photonic crystals made on a GaAs slab. Having the near infrared optical set up, photoluminescence of these quantum dots was measured and is shown in figure 1.3. The inhomogeneous broadening is due to the presence of different sizes of QDs in the solution.

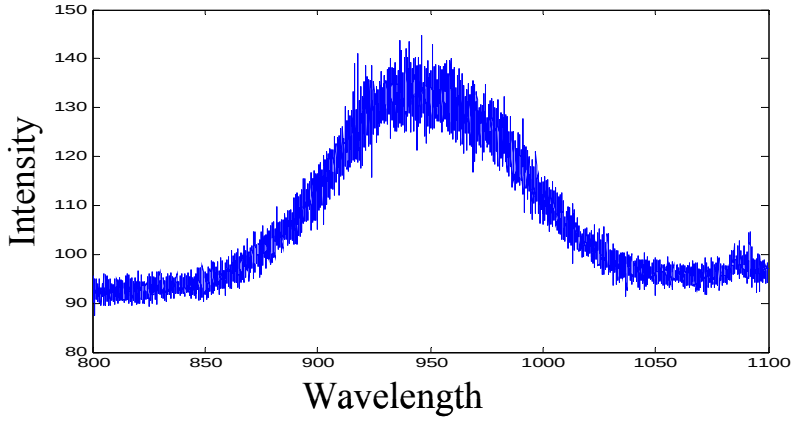

***Figure 1.3**: Photoluminescence emission of PbS nanocrystals.*

Later, Cadmium-Selenide (CdSe) quantum dots capped with a semiconductor shell of ZnS were purchased (from NN-Labs) in Toluene, where they have emission spectrum in the dark red (680nm). These QDs are considered to be the best choice of material in the visible spectrum [3]. Single CdSe QDs have a very narrow emission spectrum of 25-35nm [4] and a luminescence lifetime of 26ns [5].

Different schemes for coupling these dots to the cavities were considered. One approach was to create many cavities on the wafer and to spin coat a thin layer of QDs with the hope that one of the dots would couple to the cavity. The next approach was to further dilute the quantum dot solution with PMMA, and to use the mixture as an active layer in the cavity through a spin coating process. Mixing CdSe QDs with PMMA is discussed in [6,7]. Our effort is discussed in chapter 7.4, where green CdSe/ZnS QDs are used. The solution of dots dissolved in PMMA was very uniform and showed no signs of aggregation. Compared to the first approach, this technique seems to protect the QDs against oxidation and exposure to air, which seems to be the cause of their degradation. The final approach considered was to steer the quantum dots using

electroosmatic flow, and thus, Toluene was not a right solvent and obtaining QDs in a polar solvent was necessary. For this reason, dark red CdSe/ZnS colloidal QDs were purchased in a water solvent with concentration of $4.15\times10^{-5} mol/L$ and size distribution of 6.2-7.7nm. Figure 1.4 shows the sample placed on a stage, where it is excited using a blue LED focused by a lens. As inferred from the figure, excitation follows the light path in the solution and is very bright at the point where light comes to focus. Absorption and emission spectra of these QDs are shown in Figure 1.4, obtained from NN-labs homepage. Visualizing a single quantum dot and its manipulation in microfluid channels is discussed in chapter 4. Note that the storage of QDs was an issue and the first batch of samples purchased showed signs of aggregation after few weeks. With the vendor's recommendation, they are kept in a cold and dark surrounding (in a refrigerator) and their lid is tightly sealed to reduce their exposure to air (oxygen).

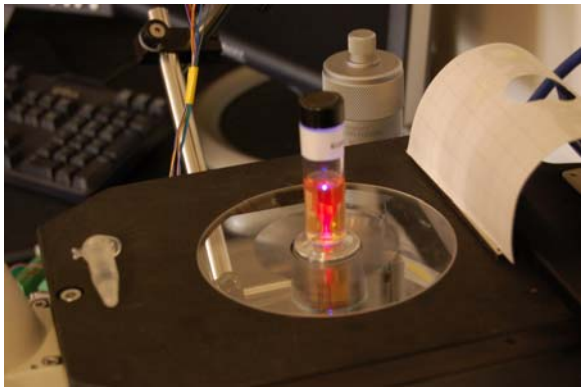

***Figure 1.4**: Sample of CdSe QDs placed on a microscope stage excited by a blue LED from the bottom surface.*

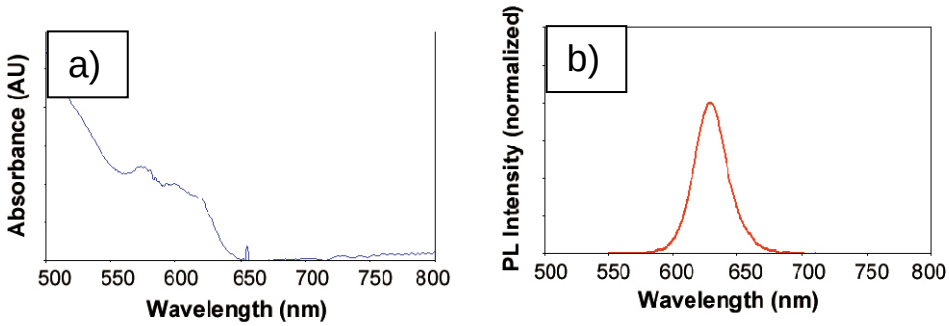

***Figure 1.5**: a) Absorption spectrum of CdSe QDs. b) Emission spectrum of CdSe QDs*

CHAPTER 2: Photonic Crystals

2.1 Introduction

The name "Photonic Crystal" and the concept of the photonic bandgap was first introduced by Eli Yablonovitch in 1989 [8]; however, the idea of a one-dimensional stop band was derived by Lord Rayleigh in 1887 [9]. These structures have become a topic of interest in the past few years with the goal of controlling the optical properties of materials. The enormous amount of research in this field has resulted in technological advancements in many areas such as communications, optics, quantum information processing, and bio-sensing. Photonic crystals are periodic dielectric structures that allow storage and wave-guiding of light through Bragg reflections. Such structures can be used to engineer cavities whose mode volumes are on the order of light's wavelength. These cavities facilitate the interaction of light with matter resulting in quantum-optical phenomena such as spontaneous emission enhancement [10], strong coupling [11], and single atom lasers [12].

Photonic crystals are usually viewed as an optical analog to solid state crystals, in that the periodic arrangement of atoms in a crystal gives rise to the energy bandgaps. These

energy bands control the motion of charge carriers through the crystal, which can be altered by adding dopants. This has led to the creation of semiconductor devices such as transistors, diodes, and semiconductor lasers. Similarly, photonic crystal cavities also have energy bandgaps that forbid the propagation of a certain frequency range of electromagnetic waves (light). Analogous to adding dopants in semiconductors, localized states within the photonic bandgaps are introduced by intentionally breaking the periodicity in adding defects or distortions to the crystal. Therefore, by engineering the properties of defects, one is capable of tuning and controlling the flow of light through the crystal.

In this chapter, we discuss silicon nitride photonic crystals for controlling and manipulating light in its visible spectrum. Having the mature silicon-based technology infrastructure present renders a very cost effective and easy fabrications procedure. In addition, silicon nitride photonic crystals are fully bio-compatible, which paves the way for applications in biological sensing. One of the main challenges is to obtain high quality factor silicon nitride cavities. This is due to a very low index-contrast between air and silicon nitride. Therefore, we discuss periodic structures and simulate cavities with high quality factors and small mode volumes. We also perform some analysis to have insights into the coupling of a QD to the photonic crystal cavity.

2.2 One-dimensional Periodic Structure

Knowing the physics of one-dimensional periodic structures is vital for understanding higher dimensional structures. Starting off with Maxwell's equations by considering a non-magnetic (μ_o=1) periodic media and a dielectric permittivity of $\varepsilon(\vec{r})$, the following equation for the field is obtained:

$$\nabla \times \frac{1}{\varepsilon(\vec{r})} \nabla \times \vec{H} = \left(\frac{\omega}{c}\right)^2 \vec{H} \qquad \textbf{(2.1)}$$

Where the electric field is given by:

$$\vec{E} = \left(\frac{-ic}{\omega \varepsilon(\vec{r})}\right) \nabla \times \vec{H} \qquad \textbf{(2.2)}$$

For a periodic medium with positive $\varepsilon(\vec{r})$, Bloch theorem[1] applies, and thus, equation (2.1) is an eigenvalue problem with orthogonal eigenstates. Consequently, the solutions are periodic fields that propagate as plane waves, given as:

$$H(\vec{x},t) = e^{i(\vec{k}.\vec{x}-wt)} \vec{H}_{\vec{k}}(\vec{x}) \qquad \textbf{(2.3)}$$

In equation (2.3), $\vec{H}_{\vec{k}}(\vec{x})$ corresponds to a unit cell, and thus, the subsequent frequencies of the field (ω) are discrete. Similar results could also be achieved for the electric field. The above analysis could be applied to a one dimensional structure as given in Figure 2.1, where $\varepsilon(\vec{r})$ could be Fourier transformed into reciprocal space[2] as: $\varepsilon^{-1}(\vec{r}) = \sum_{m=-\infty}^{\infty} k_m e^{i\frac{2\pi.m}{a}z}$ In this equation 'm' is an integer, k_m are the Fourier coefficients, and $\frac{2\pi m}{a}$ are the reciprocal lattice vectors. By considering only the components of $m = 0, \pm 1$ in the expansion of $\varepsilon^{-1}(\vec{r}) = k_0 + k_1 e^{i\frac{2\pi}{a}z} + k_{-1} e^{-i\frac{2\pi}{a}z}$ and noting that $k_{-1} = k_1^*$, one can derive:

[1] Bloch's Theorem: photons have wave properties that propagate without scattering in a periodic medium

[2] Reciprocal lattice vector b_i can be found from $b_i \cdot a_j = 2\pi\delta_{ij}$

$$\omega_{\pm} = \frac{\pi.c}{a}\sqrt{k_0 \pm |k_1|} \pm \frac{ac}{\pi |k_1|}(k_0^2 - \frac{|k_1|^2}{2})(k - \frac{\pi}{a})^2 \qquad \textbf{(3.4)} \text{ [3]}$$

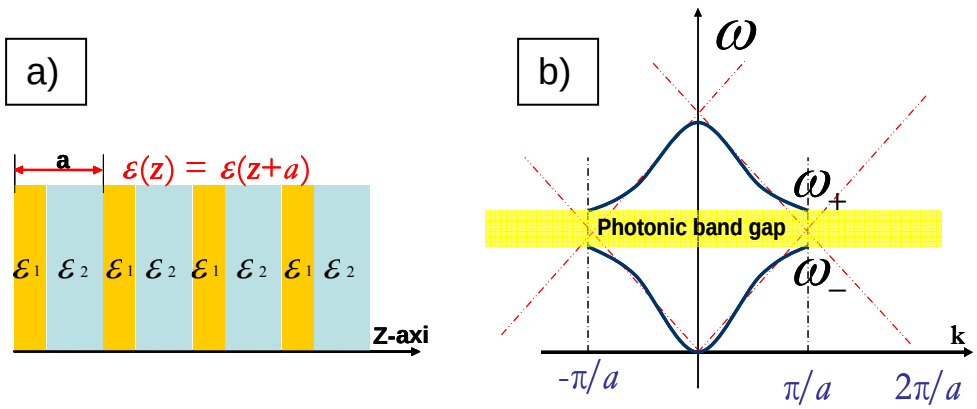

***Figure 2.1**: a) One-dimensional periodic structure. b)Photonic bandgap of the structure in figure a.*

In equation (3.4), $\Delta\omega = \omega_+ - \omega_-$, is called the photonic bandgap and is illustrated in Figure 2.1. The frequencies between ω_+ and ω_- are prohibited in this region and only evanescent waves with complex wave-vectors exist. It should be noted that the wave vectors that differ by $\frac{2\pi}{a}$ are the same and to avoid the redundancy in the calculation, one should only plot the dispersion relation over a reduced Brillouin zone[3].

It could be inferred from Figure 2.1b that the modes with k=$\pm\frac{\pi}{a}$, are mixed together in the presence of periodic modulation of the dielectric constant resulting in the frequency splitting [13]. Another way to explain this phenomenon qualitatively is to extend the electromagnetic variational theorem in a high contrast dielectric [14]. This theorem specifies that both the low-frequency and high-frequency modes concentrate

[3] Irreducible Brillouin zone is used to eliminate the redundancy in calculating the field. This finite expanse cannot be replicated by any reciprocal lattice vector while all the values of the wave vector that lie outside of this zone are accessible.

their energies in high-ε region; however, the low-frequency mode is less concentrated than the high-frequency one. Hence, the higher the contrast becomes the higher the energy bandgap would be. It should also be noted that at short frequencies (long wavelengths) the dispersion relation follows the dashed lines (where the bandgap goes to zero). This is due to the fact that at long wavelengths the wave propagation through the periodic medium does not see the dielectric constant modulation, and thus, the bandgap becomes smaller.

A question that could be raised is how the bandgap fluctuates as the propagation in the 1D periodic-crystal goes off-axis? To answer this question, one could note that the k_z remains discrete as the wave vector in z-direction sees a periodic structure; however, the k_x and k_y are continuous. Thus, there is no overall bandgap when considering an oblique beam incident on the layered crystal. To address this issue and to achieve light confinement in all directions, construction of higher dimensional photonic crystals is necessary.

2.3. Two and Three dimensional photonic crystal

Two-dimensional photonic crystals are periodic along two directions while they are homogenous along the third dimension. For light propagating in the plane of periodicity, modes could be separated into two independent polarizations known as TE and TM. The existence of the band structure and its size could vary for these modes and is completely dependent on the structure. For example, for a square lattice of dielectric columns as shown in Figure 2.2a there is a complete bandgap for the TM modes while there is no bandgap for the TE modes [13]. The situation is reversed when considering a square lattice of dielectric veins (figure 2.2c) [14]. This implies that TM bandgaps are favored

in isolated high-ε regions while the TE modes are favored in connected lattice [14]. Figure 2.2b shows the irreducible Brillouin zone calculated for a square lattice of dielectric columns. Combining the above results and predictions one can engineer a new structure with a complete and wider bandgap for both polarizations. An example of this design is the triangular lattice of air columns that is investigated in section 2.4, in details [15]. To confine light in three dimensions, these devices are made on a slab with a thickness of about $(\lambda / 2n)$. Therefore, light is confined in vertical direction through total internal reflection (due to the index contrast of the slab and the air), while its confinement in the lateral direction is controlled by distributed Brag reflections, resulting from the periodic structures.

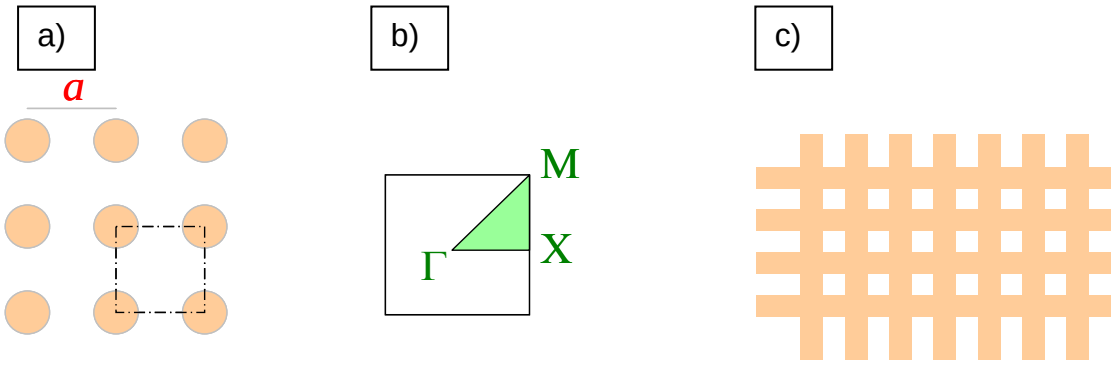

***Figure 2.2**: a) Cross-sectional view of a square lattice of a dielectric column. b) The Brillouin zone, with its irreducible part shaded in green. c) Cross-sectional view of a square lattice of dielectric veins.*

The idea of achieving a full three-dimensional photonic crystal is to control light independent of the direction of propagation. One way to realize a three dimensional photonic crystal is by taking a three-dimensional lattice and placing a sphere at each lattice point. Another way is to reverse this process by placing air bubbles at each lattice point, known as 'Inverse opal' [14]. Surprisingly, realizing a complete photonic gap is

more difficult in three-dimensional crystals, where the gap must be achieved over the entire three-dimensional Brillouin zone.

2.4 Simulation of Photonic Bandgap (MPB)

MPB software is used to calculate the modes of a periodic dielectric structure (triangular lattice of air holes). To perform the simulation we specify the geometry and the parameters and run the simulation on a UNIX based workstation. Information is then extracted from the output files. MPB, developed at MIT, is a frequency-domain numerical technique ideal for calculating photonic bandgap, which does not evolve in time. This software computes the eigenstates and eigenvalues of Maxwell's equations. Figure 2.3 and 2.4 show the obtained modes for Brillouin zone of triangular lattice of airholes for both TE and TM bands, respectively. In these 3D calculations, the slab refractive index of 2.1 is used and the hole radii are 2.5a (in simulation units). The height of the slab is also chosen to be 0.74a. The Bloch boundary condition is applied to all four sides normal to the plane of slab, and an absorbing layer is assumed at the top and bottom planes. Due to a low index contrast between the slab and airholes, the bandgap is expected to be very narrow compared to the ones reported in literature for GaAs which we calculated to be around 20%. Based on the obtained results, TM does not contain a photonic bandgap while TE has a photonic bandgap of 6.9% from $0.385\lambda_0$ to $0.4125\lambda_0$. Note, this clarifies that there is no overlapping TE/TM photonic bandgap for the triangular lattice of air holes considered for silicon nitride material. The light line indicated by red solid line in Figure 2.3 is basically the linear dispersion curve of photons in air, which differentiates between guided and leaky modes. The modes above the light line are considered to be the leaky modes, which leak energy into the surrounding air as

they propagate through the waveguide [16]. Modes below the white line are guided and confine energy as they propagate. Simulation code is provided in Appendix B.1.

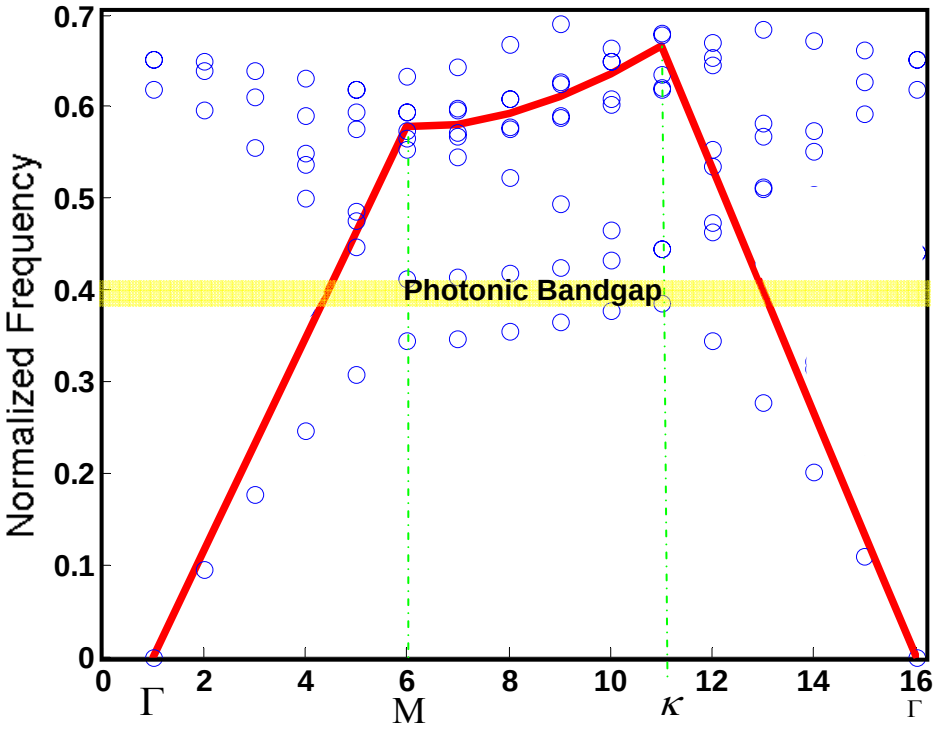

***Figure 2.3**: Modes calculated over Brillouin zone of triangular lattice of airholes for TE waves. Red solid line signifies the light line and the presence of a bandgap is indicated.*

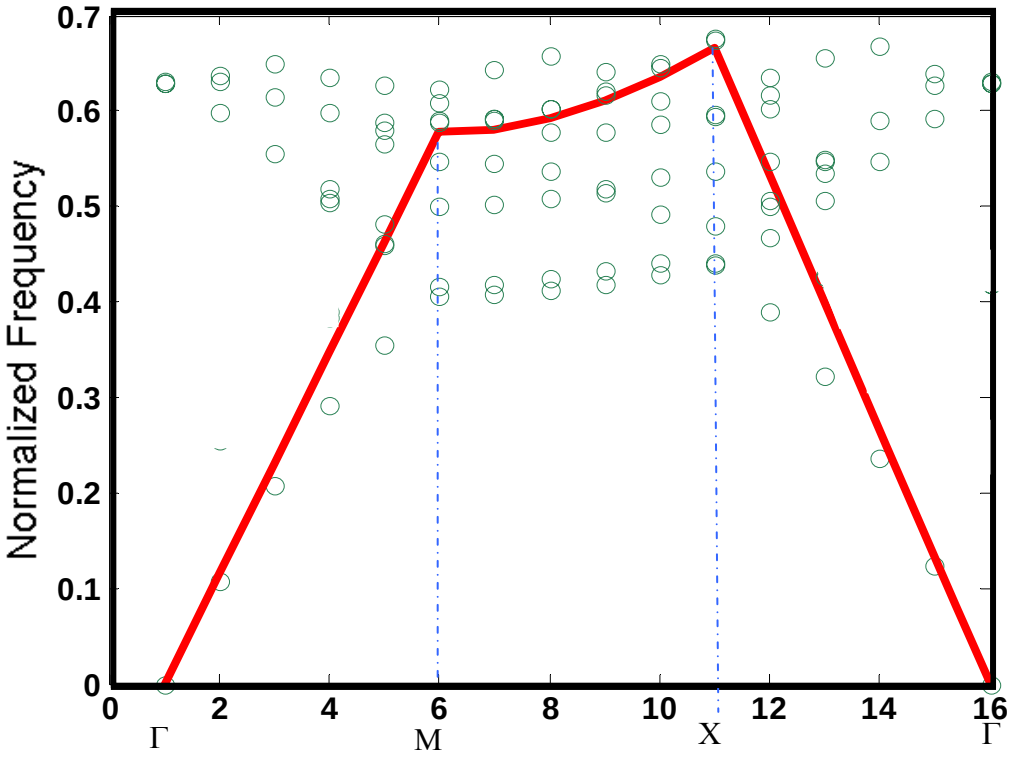

***Figure 2.4**: Modes calculated over Brillouin zone of triangular lattice of airholes for TM waves. TM modes do not experience a bandgap.*

2.4 Localized Modes at Defects

By perturbing the periodic structure in a photonic crystal, one can permit localized modes that have frequencies within the photonic bandgap. Such modes are evanescent inside the crystal while they have real wave vectors inside the perturbed region. This implies that perturbed region behaves as a cavity while the surrounding walls represent mirrors surrounding the cavity. In one-dimensional periodic structures, perturbation could be introduced, for example, by increasing the width of one layer. Doing this may lead to the existence of a mode in the photonic bandgap. A trapped mode in the cavity

(which dimensionally is in the order of light's wavelength) is similar to a microwave oscillating in a metallic cavity.

Localizing modes in higher dimensions (2D or 3D) photonic crystal is achieved by perturbing a localized site, for instance, by changing the radius of a single hole or by changing its refractive index as illustrated in Figure 2.5.

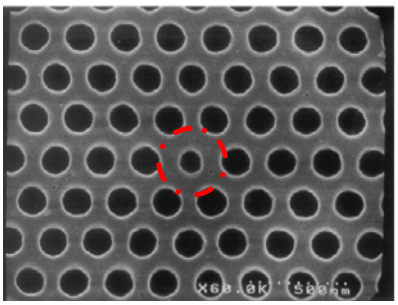

***Figure 2.5**: SEM image of the surface of a photonic crystal. Red dotted circle represents the position of the defect.*

To illustrate how a perturbation in refractive index translates to a change in the resonant frequency, one could multiply both sides of equation (2.1) by $\vec{H}^*$ and integrate over the space. By noting $\mu_o \int \vec{H} * \vec{H} d^3\vec{r} = W$ the following equation is obtained:

$$\int d^3\vec{r} \frac{1}{\vec{\varepsilon}(x)} |\nabla \times \vec{H}|^2 = \omega^2 W$$

Integrating both sides over omega: $\frac{d}{d\varepsilon}(\int d^3\vec{r} \frac{1}{\vec{\varepsilon}(x)} |\nabla \times \vec{H}|^2) = \frac{d}{d\omega}(\omega^2 W)$ leads to:

$$-\int d^3\vec{r} \frac{d\varepsilon}{|\vec{\varepsilon}(x)|^2} |\nabla \times \vec{H}|^2 = 2\omega W d\omega \qquad \textbf{(2.5)}$$

Equation (2.5) implies that by decreasing the dielectric constant, mode frequency increases, and vice versa. Consequently, for our application of constructing triangular lattice of photonic crystals on a thin membrane of silicon nitride one would expect to

have higher mode frequencies by decreasing the slab thickness and increasing the airhole radii.

Another important observation is that the perturbation (for example, missing to create some of the holes) breaks the symmetry of the structure, so modes can no longer be classified based on their wave vector. This introduces more complexity in the calculation of fields, and thus, the use of numerical techniques (such as FDTD) is inevitable when considering a 2 and 3 dimensional structures. We will analyze triangular lattice structures in section 2.5 through numerical techniques.

Based on the above description, photonic crystal structures could be engineered in such a way to guide the electromagnetic waves from one location to another one. In 2D photonic crystal geometries, light is confined in lateral directions. In these structures, a waveguide is defined simply by introducing a line of defects, for example, by removing an entire row of holes as shown in Figure 2.6 [17].

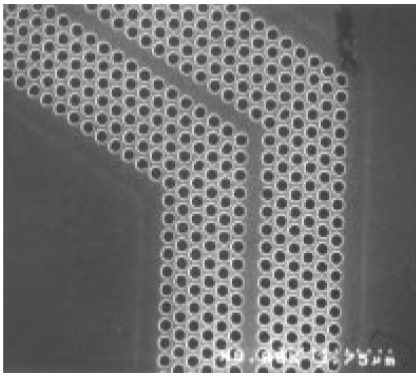

***Figure 2.6**: SEM image of a triangular structure waveguide with 60º bend [17].*

2.5 Characteristics of a Cavity

Mode volume, Purcell factors, and quality factors are some of the key terminologies in studying photonic crystal cavities. Achieving small mode volumes and high quality-

factors are vital to facilitate light-matter and photon-photon interactions in a cavity. These parameters are best realized in photonic crystal slabs compared to other cavity structures [18]. These features give rise to the spontaneous emission enhancement in the cavity compared to free space, where the ratio is known as the Purcell factor and is given by: $F = \frac{\Gamma}{n\Gamma_0} = \frac{3}{4\pi^2}\left(\frac{\lambda}{n}\right)^2 \frac{Q}{V_{mode}}$. The Quality-factor is a measure for determining how well and ideal a cavity is performing, and describes the decay rate of the electromagnetic field stored in the cavity. It is therefore defined as: $Q = \frac{\omega_0 W}{P}$, where P is the power dissipation from the cavity and W is the stored energy in the cavity. The ratio of $\frac{W}{P}$, gives the Full Width Half Maximum (FWHM) of a Lorentzian line-shape that is the Fourier transform of the electric field, where ω_0 is its center frequency. Quality factors as high as one million in silicon (by introducing a point defect inside a planar slab of photonic crystal) have been reported in the literature, where the limiting factor has been associated with the imperfections in the fabrication, such as roughness of the inner walls and the variation of the hole radii [19]. Mode Volume, on the other hand, is defined as: $V_j = \frac{\iiint \varepsilon(\vec{r})\left|\vec{E}_j(\vec{r})\right|^2 d^3\vec{r}}{\max\left\{\varepsilon(\vec{r})\left|\vec{E}_j(\vec{r})\right|^2\right\}}$, and is derived directly from the field quantization. Acquiring a very small mode volume is inherent in photonic crystal cavities.

2.6 MEEP Simulation

To calculate the quality-factor and the mode volume of photonic crystal slabs, we use Meep software that implements the finite-difference time-domain (FDTD) method for solving Maxwell's equations in time and space subject to the imposed boundary

conditions and the given geometry. Basically, modes are excited with a short Gaussian pulse at the center of the photonic crystal cavity for a short period of time. After the source is turned off, the fields bouncing inside the system are analyzed to extract frequencies and decay rates using Fourier transform tools provided by harminv. The geometries studied are triangular lattice photonic crystals having the index of 2.1 with airholes (index of 1). Cavities are made with three missing holes as shown in Figure 2.7a; hole spacing is illustrated in Figure 2.7b. Having the low index contrast, the quality-factors achieved in these structures are very low and until very recently the highest quality factors reported was 360 [20]. Playing with the hole radii and slab thickness we were able to achieve quality factors as high as 494.338 at the resonance wavelength of 0.412867 when the slab thickness and airhole radiuses were optimized to 0.7 and 0.32, respectively.

To further increase the quality factor, we tweaked the radii of two of the airholes shown in red in figure 2.7a in conjunction with optimizing other airholes radii and the slab thickness. We basically shrunk the radii of the two holes and shifted them outwards from the cavity. This is shown in figure 2.7c for the upper airhole. We have obtained quality factors as high as 3617 (refer to Appendix B.2 for the harminv output file). These simulations were performed with the following parameters $r = 0.25$, $r2 = 0.12$, and $h = 0.74$ in meep units; corresponding to, $r = 66nm$, $h = 195.5nm$, and $r2 = 31nm$.

Very recently quality-factors of 4700 have been reported in [21], where all of the airholes around the cavity are modified. Compared to our cavity design the reported design suffers from having a higher mode volume. Basically, they have achieved better quality

factors by a factor of 1.3 in expense of having worse mode volumes with the same factor; we will elaborate on this later in this section.

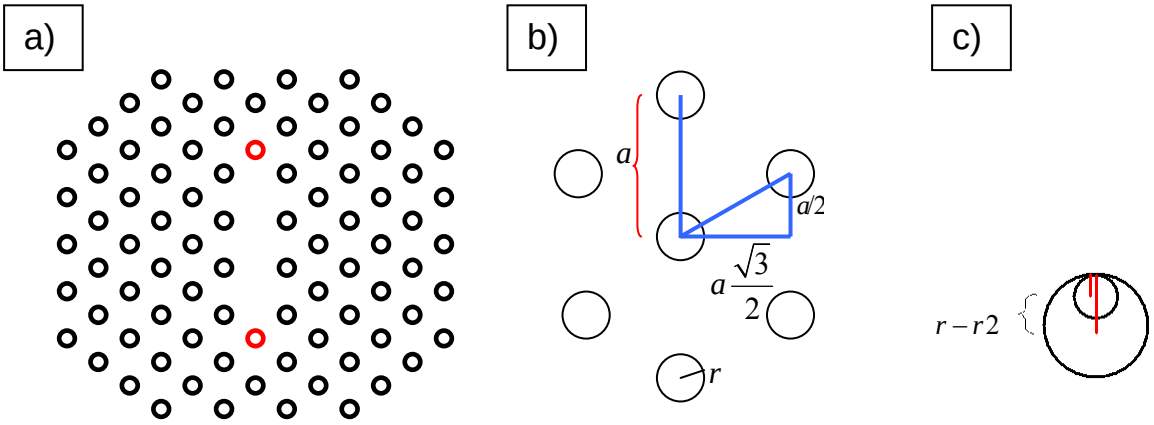

***Figure 2.7**: a) Three-hole photonic crystal cavity studied. b) Spacing of holes in the lattice. c) Modifying the top red airhole.*

One important observation is how the oscillating frequency changes when the slab thickness and hole-radiuses are modified. Simulations illustrate that by increasing the slab thickness or by lowering the airhole radii, the oscillating modes are shifted to lower frequencies. This agrees with our theoretical expectation discussed in section 2.4. Figure 2.8 shows the propagating electromagnetic fields in the slab at some times after the source is turned off. To illustrate the cavity confinement, this picture is obtained by converting the field into PNG image and the animation of the field evolution in time is also acquired. The code for this simulation is included in Appendix B.2.

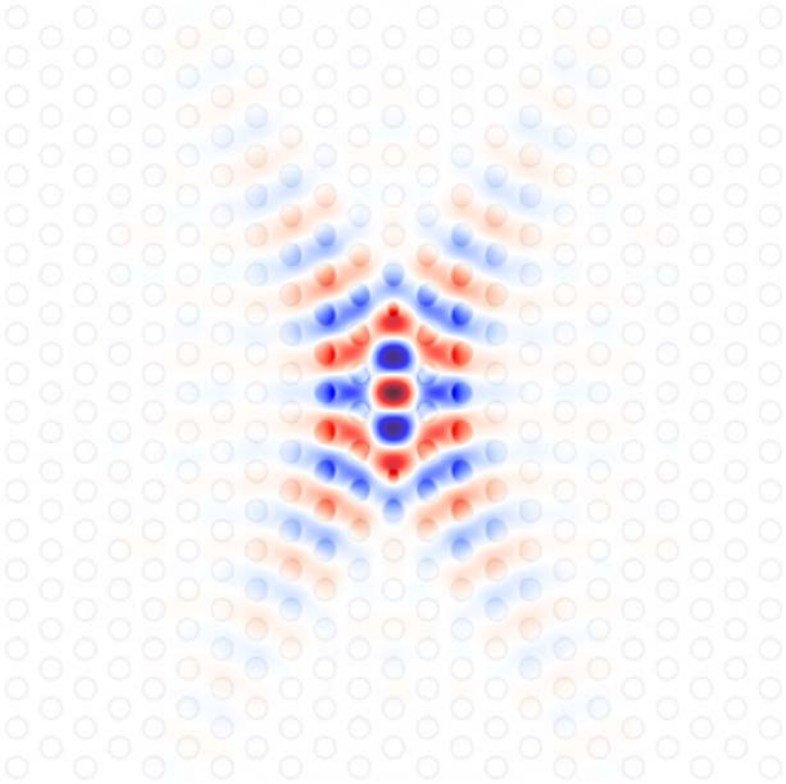

***Figure 2.8**: Oscillation of electromagnetic waves after the Gaussian source at the center of the cavity is turned off.*

In these simulations, we have excited the field by placing a source at the center of the cavity, where the field confinement is expected to be a maximum. Our goal is to determine how the field strength changes in the z-direction (when the coordinates are chosen to be at the center of the cavity). Indeed, we are interested in knowing the fraction of the field at the surface of the cavity to its value at the center. These results are crucial for our application in QD steering, where QDs are positioned at the surface of the cavity. To obtain results, we run the meep simulation with parameters that yield high quality factors, as discussed above, and output the total energy density $\left(E^{*} \cdot D/2\right)$. We choose the thickness of the slab to be 0.74 and perform the simulation with higher

resolution (resolution of 24). We calculate the mode volume by summing over all of the electric field energy and divide it with its value at the center of the cavity, taking into account the resonance frequency obtained from the simulation $(\omega = 0.38842)$. The mode volume obtained is $1.0098(\lambda/n)^3$, which is a factor of 1.3 smaller than the mode volume reported in [21] . Moreover, to view how the meep software assigns indices of refraction to discrete pixels, we plot the index of refraction at different points on the z-axis in Figure 2.9. We also show in figure 2.10, the magnitude of the field on the z-axis over its maximum value at the center $\left(\frac{|E(z)|^2}{|E_{\max}|^2} \right)$. Based on the chosen resolution and the slab thickness, the surface of the photonic crystal cavity is somewhere between points 38 to 39 where the ratio varies from 18.7% to 32.7%. Matlab code for performing this simulation is given in Appendix B.3.

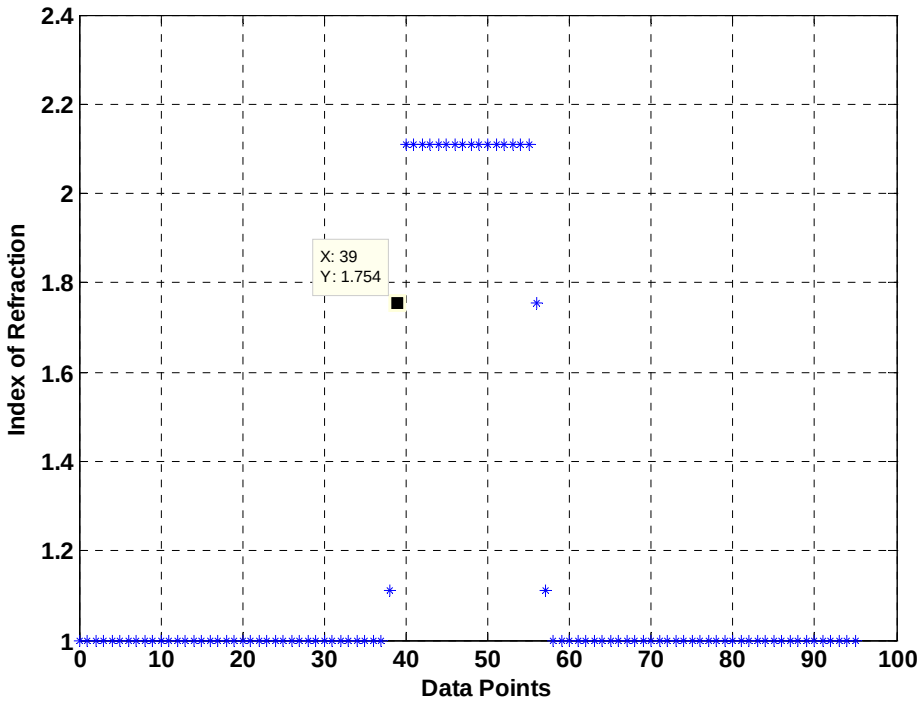

***Figure 2.9**: Index of refraction plotted on the z-axis. These points are defined by the software based on the chosen resolution for the simulation.*

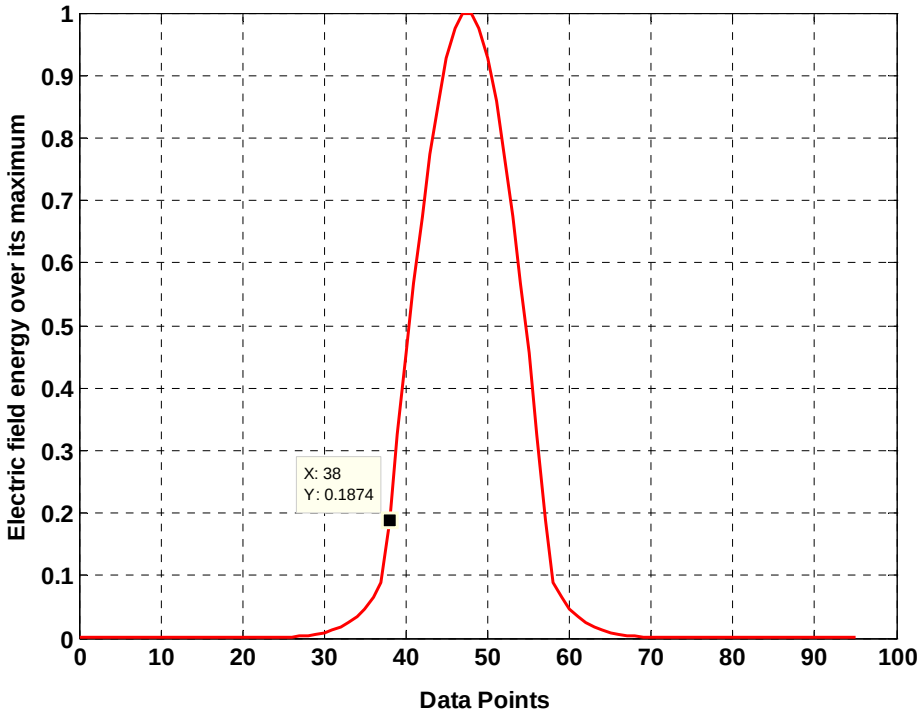

***Figure 2.10**: Magnitude of the field on the z-axis over its maximum value at the center.*

CHAPTER 3: Microdisks Resonators

3.1 Introduction

Silicon nitride microdisks are produced by etching disk-like structures standing on thin pedestals. These resonators employ total internal reflection to confine field in the planar slab, and can support very high quality whispering gallery modes. Total internal reflection occurs on the curved interface of high index (SiN_x) and low index (air), where by Snell's law the angle of incident must be greater than: $\arcsin\left(\frac{n_{SiN}}{n_{air}}\right)$. The angle of incidence can be calculated by: $\theta_i = \frac{\pi}{2}\frac{m-1}{m}$, where m (the azimuthal number) is the total number of reflections from the curved boundary before returning to the starting point

divided by 2. The presence of the thin pedestal does not perturb the field as the modes are mainly localized in the region close to the disk boundary. In addition, the thickness of the disk could be engineered to eliminate the resonance of higher order modes. An analytical approximation for calculating the modes of a microdisk is given in [22]. Silicon nitride microdisks resonators with diameter of 9μm have been reported in the literature having the quality-factor of 3.6×10^{6} and an effective mode volume of $15(\lambda/n)^3$ [23].

3.2 Simulation of Microdisks

Simulations of microdisk structures have been performed using an FDTD numerical technique that is capable of producing an accurate field distribution in complex geometries. Initially, two-dimensional simulations of disks are performed and the heights of the structures are assumed to be infinitely long in the z-direction. Quality factors as high as 193138 are achieved, when the index of 2.1 is used for a disk with dimension of $r = 1a$. The results are obtained when the disks are excited with a Gaussian source with center frequency of 1.3 and the width of 0.3 at the boundary of the microdisks. Some of the simulation results are presented in Appendix B.5, where the code for the simulation is also given. Figure 3.1 presents how the modes are confined in the cavity after some times when the source is turned off. Later, these structures were analyzed in three-dimensions (see Appendix B.6). The cross sections of the structure (with the fields) in x, y, and z are given in Figure 3.2. Further analysis should be performed to optimize the Q-factors of these cavities. For faster simulations and higher accuracies, these structures should be analyzed in cylindrical coordinates.

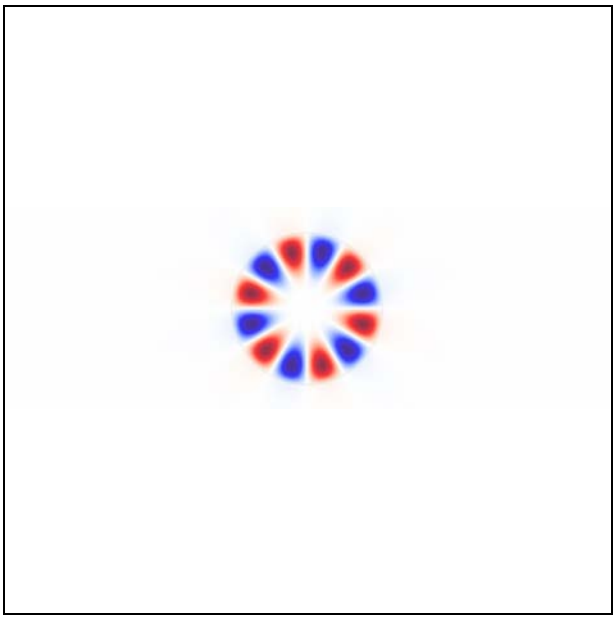

***Figure 3.1**: Two-dimensional simulation of microdisk resonators*

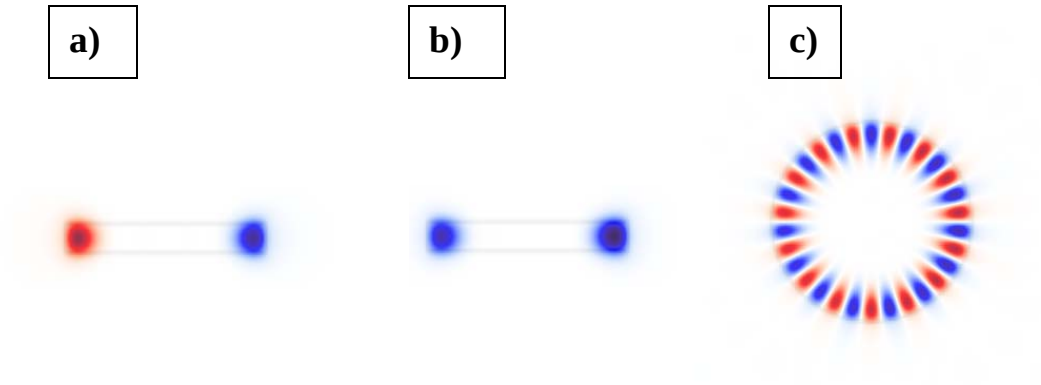

***Figure 3.2**: Three-dimensional simulation of microdisk resonators: a) x-cross section. b) y-cross-section. c) z-cross-section.*

CHAPTER 4: Positioning CdSe nanocrystals by Electroosmotically Driven Microfluidic System

4.1 Introduction

Over the past few years, significant attention has been given to steering and positioning individual particles inside microfluidic systems with the goal of creating lab-on-a-chip. Such systems are ideal for chemically treating, monitoring, analyzing, and for injecting biological materials. A variety of methods have been investigated to manipulate particles inside microfluidic systems. Amongst the most important techniques are optical tweezers, dielectrophoresis, MEMS pneumatic arrays, magnets attached to particles, and electroosmotic flow. The above techniques were analyzed for the application of placing a single CdSe colloidal nanocrystal in the center of a silicon nitride photonic crystal nano-cavity. At first sight, manipulating QDs using optical traps and laser tweezers seems to be the ideal scheme, as it offers position accuracies below tens of nanometer [24]. However, the enormous size, high cost, delicate optics required, and their functionality with only certain types of particles are only some of the drawbacks of this technique. Dielectrophoresis, MEMS pneumatic arrays, magnets attached to particles are also analyzed, but have not shown any potential for our application.

Our approach is to use a feedback control, utilizing electoroosmotic flow, in microfluidic channels. This approach to manipulating QDs is unique and has not been reported in the literature. The main advantages of this design are the capability of manipulating more than one particle at once, a minimal cost, the possibility for scaling down the design to potentially creating a hand held device, and a simplistic design architecture. Steering colloidal CdSe nanoparticles has been performed in collaboration

with Ben Shapiro's research group, based on their on-going work in steering particles on micro-size dimensions [25&26]. The basic idea is to determine the particles position and to apply enough force at each time step, in order to move the particles to the desired locations. The accuracy of this approach is limited by the resolution of optical imaging and the Brownian motion that particles experience in-between flow control corrections [26]. This approach can be extended to applications in biological sensing where the biological-cells are tagged by fluorescent QDs and are manipulated in microfluidic channels or in velocimetry where the speed of liquid in the channel is determined [27].

4.2 Electroosmotic Flow

Electroosmotic flow (EOF) is the motion of ions in a solvent environment, where the ion migration is facilitated through an applied potential difference across the two ends of a channel. The potential difference applied originates in an electrical double layer at the stationary/solution interface. The inner surfaces of the poly(dimethylsiloxane) (PDMS) is negatively charged due to the creation of $Si\text{-}OH^-$ on the surface. Negatively charged layer is known to be associated with the pH of the solvent in the experiment [28], which is about 7.0. The negative charges on the wall attract the cations in the solvent, which congregate adjacent to the negatively charged layer. The double layer created resents a frictionless interface between fluid and glass surface. Therefore, when a potential difference is maintained across the channel, with an anode at one end and a cathode at another, the solvated cations will migrate towards the cathode. This migration of cations drags the rest of the solution (even anions) by viscous force from the cathode to the anode. This mechanism of transporting fluid in microfluidic channels leads to a flat flow profile, when compared to a parabolic profile observed in a pressure-driven flow. Figure

4.1 illustrates two mechanisms of transporting fluid. One mechanism is Electroosmotic flow (as explained above) is due to the transport of particles with the liquid, whereas electrophoresis flow is the movement of ions due to the applied potential. The net flow is shown on the figure and has a flat profile [29].

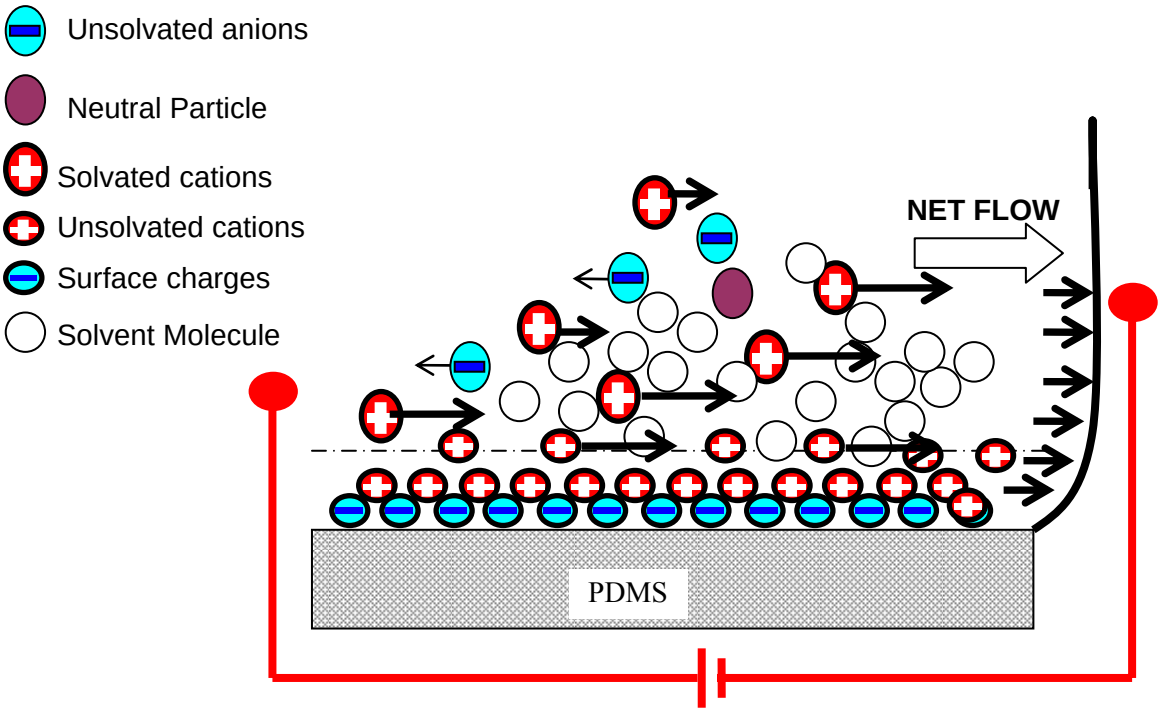

***Figure 4.1**: Mechanisms of fluid flow when a potential difference is applied across the two end of a micorchannel.*

4.3 Governing Equations in Microfluidic and control Algorithm

The classical study of the fluid dynamics is based on the assumption that the fluid can be considered a continuum, i.e. its density, velocity and pressure are defined everywhere in the space and vary continuously from point to point. This assumption is valid even at the micro-scale whenever the dimensions are larger than 10nm, below which an analysis at molecular level is more appropriate [30]; having the smallest dimension of our system

in the order of the micrometer, the classical theory is applicable. When the continuum assumption holds, the governing equations are the conservation of mass, momentum and energy, which form a set of partial differential equations that can be extremely complicated to solve. However, by assuming a constant fluid temperature across the channel, having an incompressible liquid, and operating in a low Reynolds number, the conservation equations reduce to the well-known Navier-Stokes equations for incompressible laminar flow:

$$\rho\left(\frac{\partial \vec{u}}{\partial t} + \vec{u}\cdot\nabla\vec{u}\right) - \nabla\cdot(\mu\cdot\nabla\vec{u} + \nabla\vec{u}^{T})) + \nabla p = \vec{F} \qquad \textbf{(4.1)}$$
$$\nabla\vec{u} = 0$$

Where $\vec{u}$ is the velocity field, p is the pressure, and $\vec{F}$ is the sum of the external forces applied to the fluid [30]. The only relevant external force is the electric field applied across the channel. Combining the force created by the electric field and the Navier-Stokes equations and imposing the slip boundary condition result in a linear relationship between the liquid velocity and the applied potential. Electric field imposed is basically the potential difference across the two ends of a channel over the channel length. The reduced equation is given by [26]:

$$\vec{V}(x,y) = \frac{\varsigma\varepsilon}{\eta}\vec{E}(x,y) \qquad \textbf{(4.2)}$$

Where, ε is the permittivity of the liquid, η is its dynamic viscosity, and ς is the zeta potential at liquid/solid interface. The coefficient in front of the electric field, $\frac{\varsigma\varepsilon}{\eta}$, is assumed to be a constant. Having a linear relationship between the electric field and the particle velocity, a control algorithm is designed that takes advantage of the superposition principle to exert forces and to control the dots in the planar view.

4.4 Locating and Positioning CdSe Nanocrystals in Real-Time

As discussed in section 1.2, CdSe QDs posses very small dimensions and could not be observed by an optical microscope; however, their location could be determined through the light that they emit. Having this in mind, quantum dots are excited in the microfluidic channels, using the collimated light of a blue LED [465nm, Luxeon], and are observed under the optical microscope with a numerical aperture of 0.6 and a 40x objective. To achieve a higher imaging resolution, the objective is fixed in such a way that the channels are viewed from the bottom surface. The signal is then passed through a high-pass filter to isolate the photons emitted from quantum dots [long pass filter 600nm, Thorlabs]. A camera [VC2038 Vision] is employed that is capable of obtaining 40 frames per second and is directly connected to a computer through a Matlab interface. The camera is slow enough to detect enough photons for locating a QD and fast enough so that it could track the dot's trajectory. Typically, 10000 photons per second are emitted from a single CdSe QD [31], so in practice, defining the position of the quantum dot requires at least one millisecond of photon collection. Through image processing, the positions of particles are established and are compared to their destination. Accordingly, the results are fed into a control unit that computes the electrode voltages that create the desired particle velocities. In addition, this unit corrects for the errors using a non-linear feedback loop presented in [25]. Consequently, actuators (electrodes) create the required flow to move the particles on the desired trajectory. This sequence repeats on every time-step. The schematic of this design is shown in Figure 4.2.

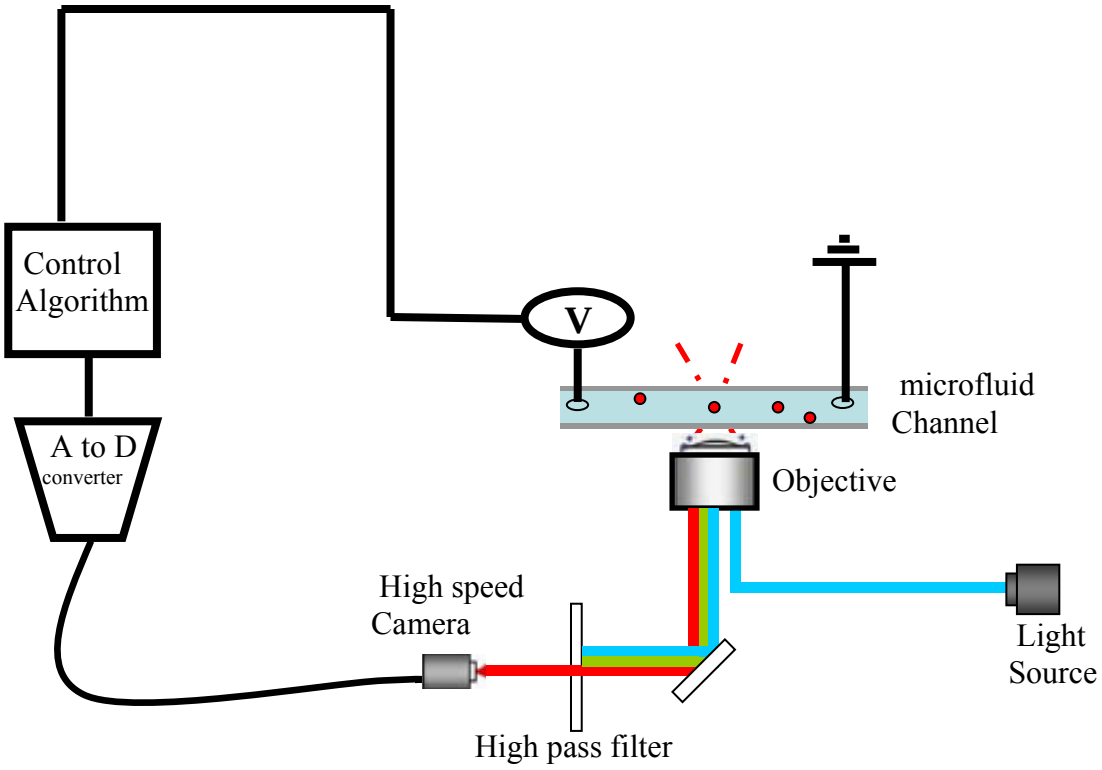

***Figure 4.2**: Experimental set up for manipulating QDs.*

4.5 Experiment Setup

4.5.1 Creating Microchannels in PDMS:

PDMS microchannels are created through a process of replication molding reported in [26]. The crossed-channel mold was created using optical lithography and using SU8 as the photoresist. The patterns of SU8 created on a Silicon wafer are 11μm tall with a width of 50μm. The solution of PDMS is produced and poured on the wafer with a thickness of approximately 3mm. PDMS is then cured at room temperature for 24 hours in a contained Petri dish. A razor blade is used to cut out the sections of PDMS with cross channels, which is consequently peeled off using a pair of tweezers. Microscope slides (later replaced by Silicon Nitride membranes) are used as the bottom surface. To create reservoirs and inserting the actuators, holes with diameter of 10mm were stamped

on the channel (about one centimeter away from the crossing point). A schematic of the cross-channel produced is shown in Figure 4.3.

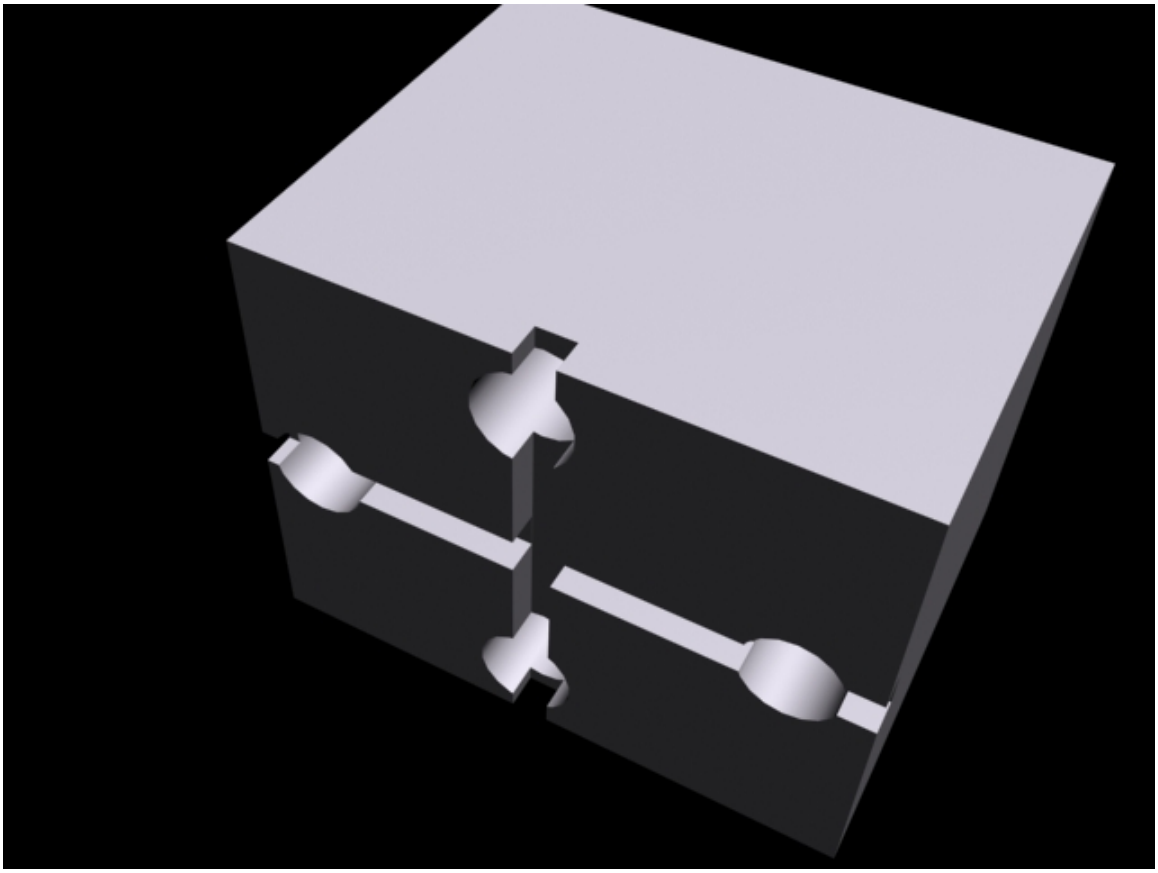

***Figure 4.3**: Schematic of a peeled off cross-channel of PMMA.*

4.5.2 Creating flow in the channels:

The quantum dot solution was mixed with the photoresponsive liquid (section 4.6) and de-ionized water to achieve concentrations yielding a few quantum dots in the control chamber, with a proper viscosity. A small drop of Ethanol was used to make the channels hydrophilic, and to consequently, fill the channels easily. One reservoir was filled with the prepared solution of quantum dots (using a pipette) and microfluid channels were filled by applying suction to the other reservoirs. Once the channels were filled, other reservoirs were filled to approximately the same height as the first reservoir

in order to equalize the pressure in the channels. The device is then placed on the microscope stage, which is focused and stigmated on the control area. The platinum electrodes are then inserted into the reservoirs by hand and particle steering is performed by applying potential differences up to ± 10 volts. A cartoon of the electrodes and PDMS placed on a slab of PC cavity and a red sphere representing a QD is shown in Figure 4.4.

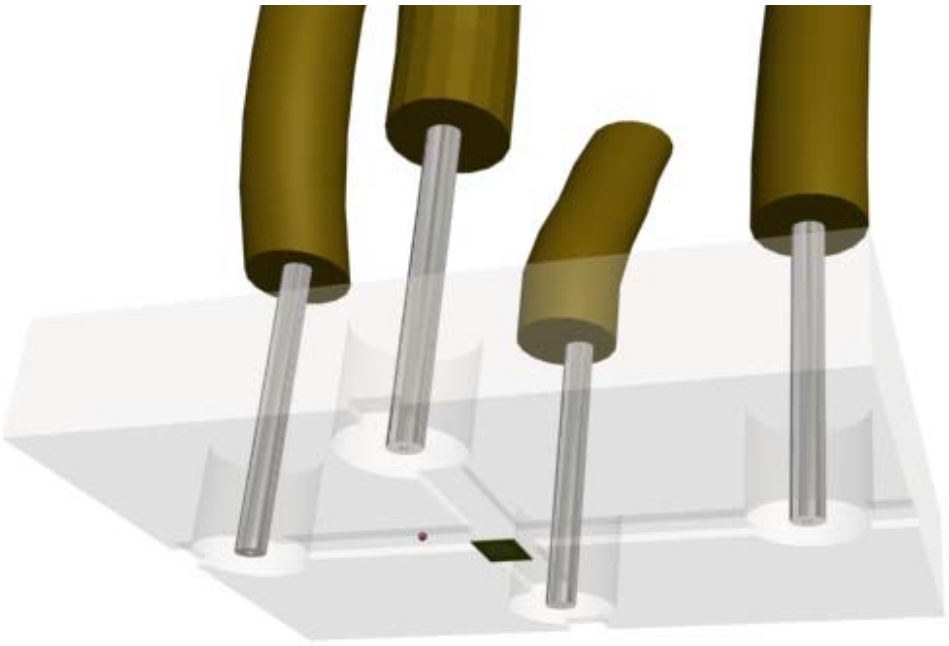

***Figure 4.4**: Schematic of the setup for particle steering in the cross-channels.*

4.5.3 Result and Discussion

As moving micron-size beads was demonstrated by Ben Shapiro's group [25], we initially mixed CdSe quantum dots with the bead solution and performed the particle steering on the beads. Then by utilizing a camera with a higher resolution and by modifying its properties, such as increasing the gain and adjusting the frame rate, in conjunction with a high-pass filter, we were able to visualize the quantum dots in the solution. A black plastic object was used to cover the microfluidic channel in order to reduce the background noise. In addition, a thinner microscope slide was used for better

accuracy in visualizing the particles. An image of the fluid channel with CdSe quantum dots and the beads is shown in Figure 4.5.

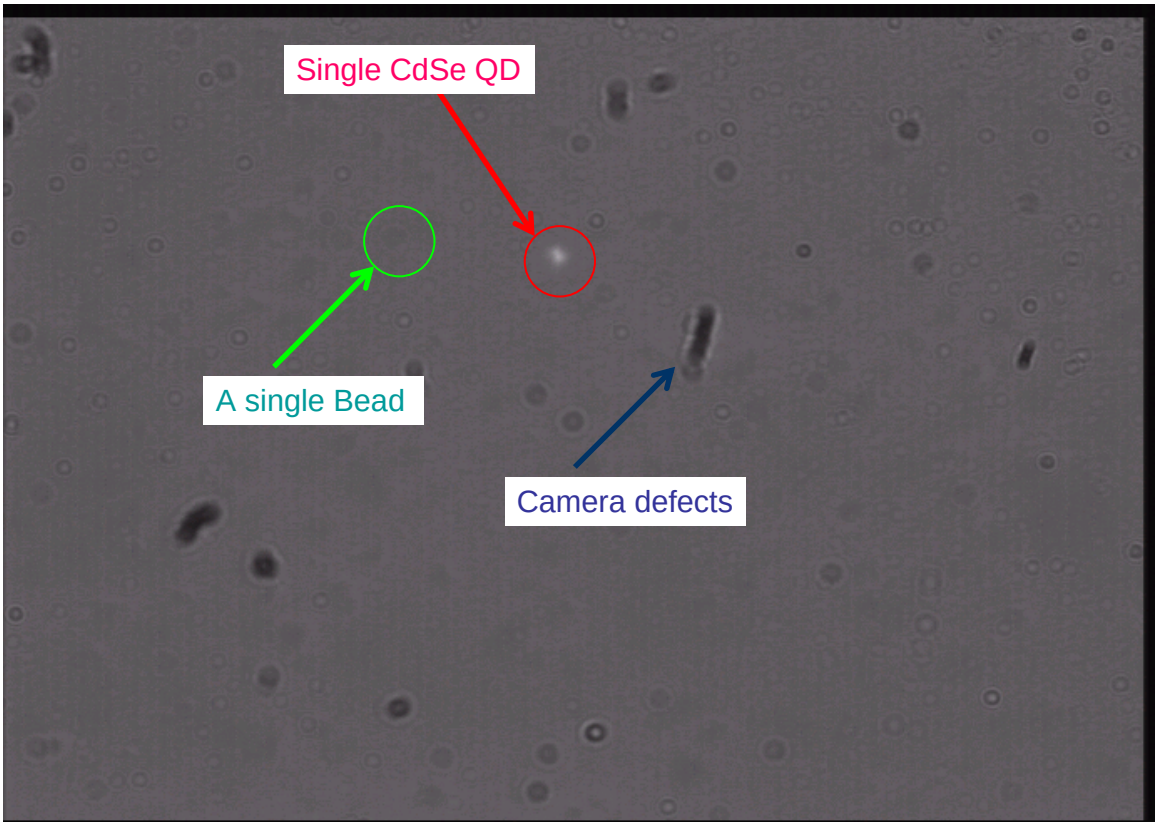

***Figure 4.5**: An image of the fluid channel with single beads and quantum dots.*

The initial experiments were performed using quantum dots in water solution, and suffered greatly from unequal pressure differences in the reservoirs. The pressure difference in the reservoirs contributed to the particles being accelerated with very high speeds (with the liquid flow). For this reason, a more sophisticated optical mask for creating fluid channels were designed, which is shown in Figure 4.6. The geometry of this mask contributes to a very stable system. Figure 4.7 shows the schematic of magnified cross-section of the channels placed on a membrane of a photonic crystal cavity.

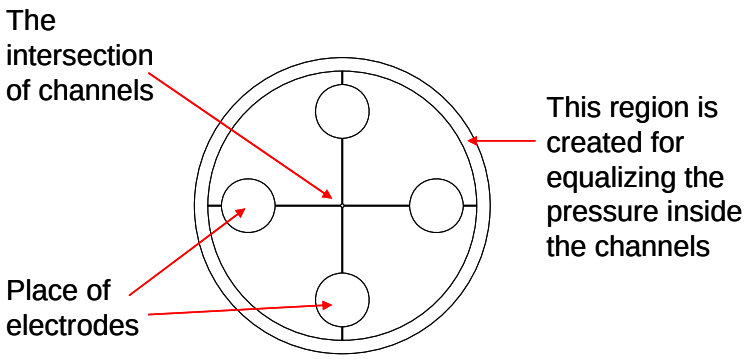

***Figure 4.6**: Mask designed for equalizing the pressure in the channels.*

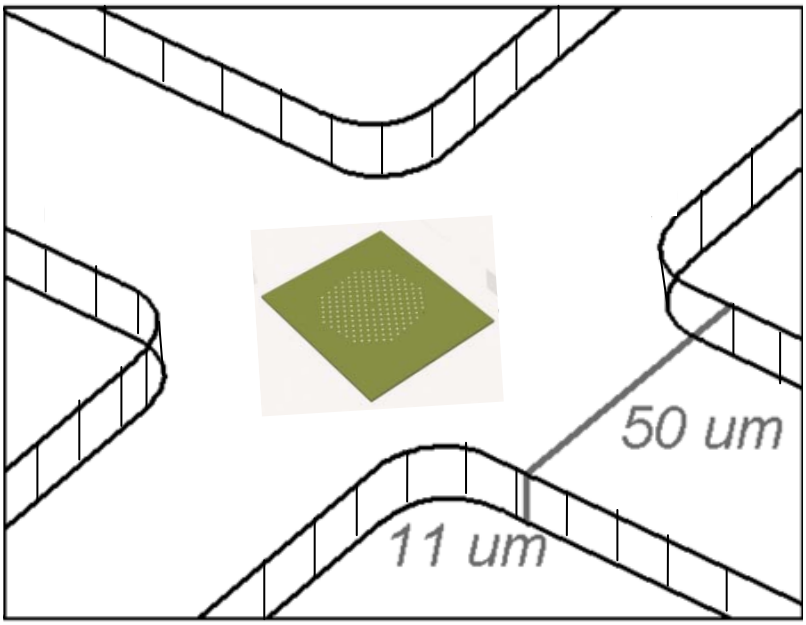

***Figure 4.7**: Schematic of the cross-section of PMMA with respect to a membrane of a photonic crystal cavity.*

Another approach for having slower flow rates in the control chamber and the channel is to increase the solution's viscosity. As explained above, our light sensitive liquid could be made at any concentrations, and thus, mixing a concentration where it is possible to fill the channels and to achieve slow flow rates is optimal. Other advantage of using a more viscous solution is less time needed to solidify the quantum dot at the center of a cavity (see section 4.6). The most viscous solution used for filling the channels and performing particle steering had the viscosity of 0.1, which is 100 times more viscous than water. Performing experiments with this viscosity demonstrated much simpler control and positioning.

Figure 4.8 shows an image of a channel placed on a silicon nitride membrane. We performed an experiment and confirmed that electroosmotic flow is possible on the silicon nitride membrane. By applying voltages across the channels we were able to speed up or reverse direction of flow in the channel.

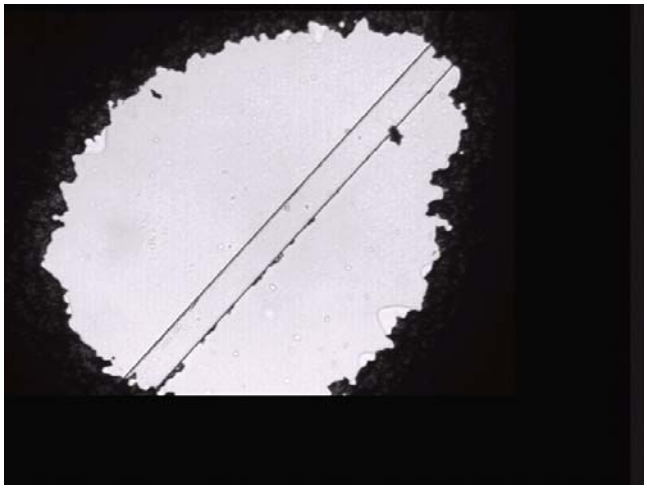

***Figure 4.8**: Microscopic image of a channel placed on a silicon nitride membrane to prove electroosmotic flow on the surface of silicon nitride.*

Figure 4.9, is a snap shot of a QD inside a microfluidic channel, where the circle around the QD is made by our control algorithm verifying that the position of the QD is detected. We have shown that it is possible to control the movement of a QD inside the microfluidic channels (in x and y direction) and have demonstrated the possibility of holding a QD at a position. In addition, we know that the solution could be made to have very high viscosities when treated by UV light. Therefore, one could bring a quantum dot to the center of a photonic crystal cavity and by holding it and using a UV laser to solidify the liquid locally. This process could be repeated, to bring and localize quantum dots at the center of photonic crystal cavities. Extending this scheme to control multi-quantum dots is possible. However, more channels are required to control multiple dots at the same time. Additional channels introduce higher degrees of freedom into the system, and therefore, creating more complex flow fields to carry dots is feasible. Steering three bead particles using eight channels is presented in [26]. Combining their algorithm with our set up for moving quantum dots, it is feasible to bring three different quantum dots to the center of cavities and treat the solution with UV light, while keeping the dots stationary.

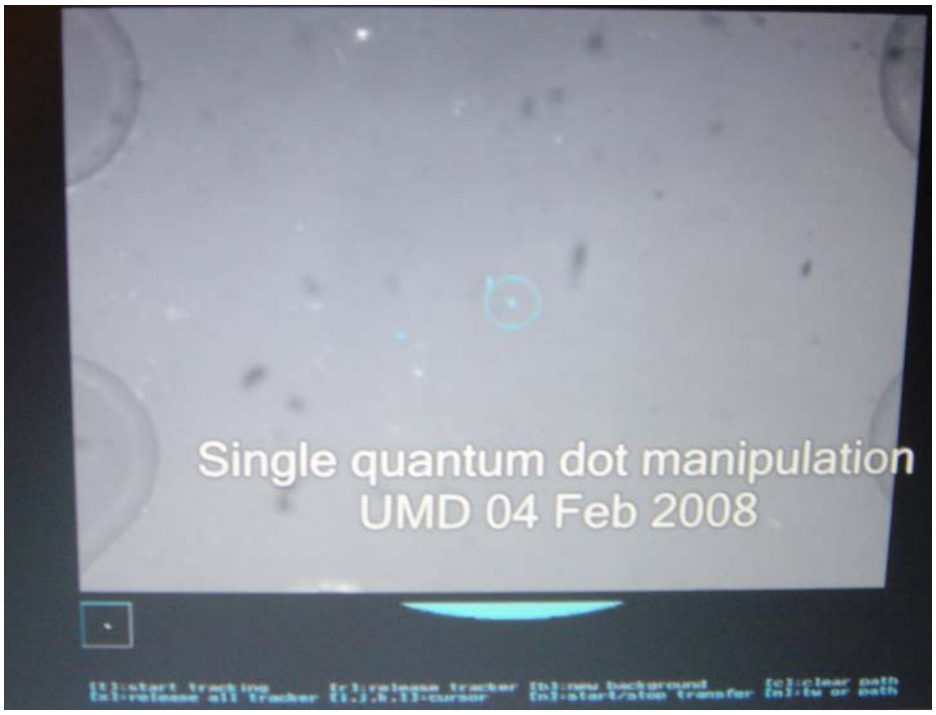

***Figure 4.9**: Image of a CdSe QD being detected and manipulated.*

4.6 Photoresponsive Fluids

In these experiments, we take advantage of fluids whose viscosity can be tuned by light. This work is in collaboration with Rockesh Kumar, whose work is presented in [32]. The idea is to increase the viscosity and freeze the kinetics of CdSe QDs after they are moved to their final destination. To tune the viscosity, the idea is to exploit molecular self-assembly, i.e., the spontaneous aggregation of surfactant or polymer molecules when placed in a solvent. Initially, the molecules in the fluid self-assemble into discrete spherical nanostructures, which impart a low viscosity to the sample. Under the action of the stimulus (light), the self-assembly is switched such that the molecules form a connected network of chains, and the sample in turn, exhibits a high viscosity. Hence,

the transition in macroscopic properties is coupled to those at the nanostructural and molecular levels.

CHAPTER 5: Energy Transfer between Two QDs in a Cavity

5.1 Introduction

Over the past several decades, there has been a widespread effort to calculate rates of energy transfer between two chemical species. This has been important in applications such as analytical chemistry, protein conformation studies, DNA detection, and biological assays. Two distinct mechanisms of radiative and non-radiative transfer have been known to mediate this process. Studies have revealed that both processes are distance dependent. In the near zone non-radiatvie Förster transfer dominates and is characterized by an R^{-6} distance dependence in the limit where the coupling between donor and acceptor is weak enough, while in the far zone radiative transfer dominates and is dependent on distance by R^{-2}. A unified theory of radiative and non-radiative energy transfer between a donor and acceptor pair in vacuum is given in [33]. However, there have been limitations in the energy transfer and its efficiency between a donor and an acceptor and for this reason, modification of the energy transfer rate between an excited and an unexcited atom subject to the environment has been reported in [34]. Here, we are investigating a system of a donor and an acceptor coupled to an optical cavity, as illustrated by a cartoon in figure 5.1. We present a formulism for calculating the efficiency and the transfer rate between a donor and an acceptor that are assumed to have only two states of energy, and we find it crucial to use a full quantum mechanical description of the field interacting with atoms. This derivation is very similar to the one atom cavity interaction presented in [1].

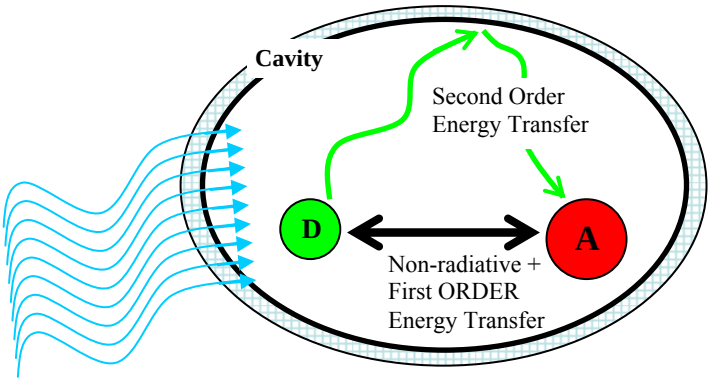

***Figure 5.1**: Animation of two QDs placed in a cavity.*

5.1 Formulating the energy transfer and its efficiency

This formulism considers the second order energy transfer where the donor puts one photon in the cavity, which is then captured by the acceptor. We ignore the non-radiative and the first order processes, where the donor and acceptor are directly excited by the external sources. We basically assume a situation where the acceptor and donor are spaced apart, and thus, their coupling is negligible. One of our motivations for analyzing this model is to use it for creating a biosensor for chemical detection with better accuracy than the conventional FRET scheme [35]. Our next motivation in understanding the physics of energy transfer in a photonic cavity is to create enhancement in emission of the donor as reported in [36] with one dimensional cavities, for creating a more powerful single photon source. To realize this in practice, one can use a green and a red CdSe quantum dot to represent a donor and an acceptor, respectively. In addition, photonic crystal cavities or microdisks are excellent candidates for cavities. To give a better insight into the problem, the whole system can be modeled as a mass-spring system, as shown in figure 5.2.

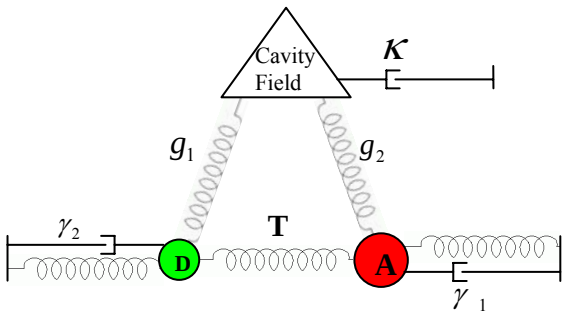

***Figure 5.2**: Mass spring model of coupling two QDs to the cavity mode.*

We start by writing the Hamiltonian for a donor-acceptor pair coupled to an optical microcavity. Note that the interaction terms are treated as perturbations of the system.

$$H = \underbrace{H_{rad} + H_{mol}(D) + H_{mol}(A)}_{H_o} + \underbrace{H_{\text{int}}(D) + H_{\text{int}}(A) + \overbrace{H_{\text{int}}(DA)}^{\text{nonradiative or first order contribution (Not considered)}}}_{V}$$

$$= \hbar\omega_0 b^+ b + \frac{1}{2}\hbar(\omega_0 + \delta_1)\sigma_z^1 + \frac{1}{2}\hbar(\omega_0 + \delta_2)\sigma_z^2 + \hbar g_1\left(\sigma_1^+ b + \sigma_1^- b^+\right) + \hbar g_2\left(\sigma_2^+ b + \sigma_2^- b^+\right) \quad \textbf{(5.1)}$$

Where b represents the field operator while σ is the dipole operator with 1 and 2 indices representing donor and acceptor, respectively. We also assume that the cavity is excited by a weak monochromatic field with frequency ω_0, and we let: $\sigma_z^1 = \sigma_z^2 = |e\rangle\langle e| - |g\rangle\langle g| = -1$. δ_1 and δ_2 are the detuning of donor and acceptor from the cavity field and g_1 and g_2 represent the dipole coupling to the cavity. We also introduce κ as the cavity decay rate given by ω_0/Q, and γ_1, γ_2 as dipoles decay rate due to losses associated with coupling to other modes than the cavity mode and the non-radiative decay rate (for donor and acceptor).

From the Hamiltonian, the equations of motion for the field, donor, and acceptor are obtained as follows:

$$\begin{cases} \dot{b} = -(i\omega_0 + \kappa)b - ig_1\sigma_1^- - ig_2\sigma_2^- \\ \dot{\sigma}_1^- = -\left(i\omega_1 + \gamma_1\right)\sigma_1^- - ig_1 b \\ \dot{\sigma}_2^- = -\left(i\omega_2 + \gamma_2\right)\sigma_2^- - ig_2 b \end{cases} \quad \textbf{(5.2)}$$

Letting:

$$b = Be^{-i\omega_0 t}, \sigma_1^- = De^{-i\omega_1 t}, \sigma_2^- = Ae^{-i\omega_2 t}, \delta_1 = \omega_1 - \omega_0, \delta_2 = \omega_2 - \omega_0$$

The above set of equations becomes:

$$\begin{cases} \dot{B} = -\kappa B - ig_1 De^{-i\delta_1 t} - ig_2 Ae^{-i\delta_2 t} \\ \dot{D} = -\gamma_1 D - ig_1 Be^{i\delta_1 t} \\ \dot{A} = -\gamma_2 A - ig_2 Ae^{i\delta_2 t} \end{cases} \quad \textbf{(5.3)}$$

Solving 5.3 (which is a first-order differential equation) for B gives:

$$B = e^{-\kappa t}\int_0^t e^{\kappa t}\left[-ig_1 De^{-i\delta_1 t} - ig_2 Ae^{-i\delta_2 t}\right]dt + B_0 e^{-\kappa t}$$

$$= -ie^{-\kappa t}\left[\frac{g_1 De^{(-i\delta_1+\kappa)t}}{-i\delta_1 + \kappa} + \frac{g_2 De^{(-i\delta_2+\kappa)t}}{-i\delta_2 + \kappa}\right] + B_0 e^{-\kappa t} \quad \textbf{(5.4)}$$

This equation simplifies to the following by assuming no initial field present:

$$\Rightarrow \boxed{B = \frac{-ig_1}{-i\delta_1 + \kappa} De^{-i\delta_1 t} + \frac{-ig_2}{-i\delta_2 + \kappa} Ae^{-i\delta_2 t}} \quad \textbf{(5.5)}$$

Solving for D and A by plugging B into equation 5.3 gives:

$$\dot{D} = -\gamma_1 D - ig_1\left(\frac{-ig_1}{-i\delta_1 + \kappa} De^{-i\delta_1 t} + \frac{-ig_2}{-i\delta_2 + \kappa} Ae^{-i\delta_2 t}\right)e^{i\delta_1 t}$$

$$D = D_0 e^{-\gamma_1 t} + e^{-\gamma_1 t}\int_0^t e^{\gamma_1 t}\left[-\frac{g_1^2 DB}{\kappa - i\delta_1} - \frac{g_1 g_2 AB}{\kappa - i\delta_2} e^{i(\delta_1 - \delta_2)t}\right]dt$$

$$= D_0 e^{-\gamma_1 t} - \frac{g_1^2 DB}{\gamma_1(\kappa - i\delta_1)} e^{\gamma_1 t} - \frac{g_1 g_2 AB}{(i(\delta_1 - \delta_2) + \gamma_1)(\kappa - i\delta_2)} e^{(i(\delta_1 - \delta_2) + \gamma_1)t} \quad (5.6)$$

Similarly,

$$\dot{A} = -\gamma_2 A - ig_2\left(\frac{-ig_2}{-i\delta_2+\kappa}Ae^{-i\delta_2 t} + \frac{-ig_1}{-i\delta_1+\kappa}De^{-i\delta_1 t}\right)e^{i\delta_2 t}$$

$$\Rightarrow A = A_0 e^{-\gamma_2 t} - \frac{g_2^2 AB}{\gamma_2(\kappa - i\delta_2)}e^{\gamma_2 t} - \frac{g_1 g_2 DB}{(i(\delta_2-\delta_1)+\gamma_2)(\kappa - i\delta_1)}e^{(i(\delta_2-\delta_1)+\gamma_2)t} \qquad (5.7)$$

This is a second-order transition process where the donor $(|D\rangle)$ makes an energy nonconservative transition to the cavity $(|m\rangle)$ and cavity makes another energy nonconservation transition to $(|A\rangle)$. However, overall energy transfer in the process is conserved [37]. This energy transfer is given by Fermi's Golden Rule:

$$w_{D\to A} = \frac{2\pi}{\hbar}\left|\overline{\sum_m \frac{V_{Am}V_{mD}}{E_D - E_A}}\right|^2 \rho(E_A)\Bigg|_{E_A \simeq E_D} \qquad \textbf{(5.8)}\ [37]$$

Or more commonly,

$$w_{D\to A} = \frac{2\pi}{\hbar}\left|V_{AD}\right|^2 \delta(E_D - E_A) \qquad \textbf{(5.9)}$$

$\rho(E_A)$ is the acceptor's final density of states. To solve this problem, only one intermediate state is assumed. It is also assumed that E_D and E_A are equal but the acceptor decays with the decay rate of Υ to $\hbar\omega_2$ (shown in Figure 5.3). Therefore, $E_D - E_A = i\Upsilon$.

$$W_{FI} == \frac{2\pi}{\hbar}\left|\frac{\langle DA^*,0\,|\,DA,1\rangle\langle DA,1\,|\,D^*A,0\rangle}{E_D - E_A}\right|^2 \delta(E_D - E_A) = \qquad \textbf{(5.10)}$$

$$\frac{2\pi}{\hbar}\left|\frac{g_2^2}{\gamma_2(\kappa - i\delta_2)}\frac{g_1^2}{\gamma_1(\kappa - i\delta_1)}\right|^2 \frac{1}{\Upsilon^2}$$

These results state that having a good coupling to the cavity for donor and acceptor, one can increase the transition rate of photons from the donor to the acceptor. These results

are very similar to the second order time-dependent perturbation theory obtained in [38], if applied to cavities with one mode.

Furthermore efficiency in transferring a photon from Donor to Acceptor could be calculated as follow:

$$E = \left| \frac{\langle \psi | AA^* | \psi \rangle}{\langle \psi | D^* D | \psi \rangle} \right| = \left| \frac{\frac{g_2^2}{\gamma_2(\kappa - i\delta_2)}}{\frac{g_1^2}{\gamma_1(\kappa - i\delta_1)}} \right| = \left| \frac{g_2^2 \gamma_1(\kappa - i\delta_1)}{g_1^2 \gamma_2(\kappa - i\delta_2)} \right| \qquad \textbf{(5.11)}$$

Therefore, when there is no detuning and the decay rate of donor and acceptor are equal, efficiency is given by the ratio of the coupling of the acceptor to the cavity over the coupling of the donor to the cavity. The results makes sense when is compared to the mass-spring analogy. Basically, force is transferred perfectly when the two spring are identical. This seems to be less sensitive when compared to the efficiency of FRET which is given by: $\phi \propto \left(\frac{R_0}{R} \right)^6$. In this equation, R is the distance between a donor and an acceptor while R_o is the critical separation when the rate of energy transfer (κ_{ET}) is equal to the rate of radiative (κ_{ET}) plus nonradiative (κ_r) energy transfer.

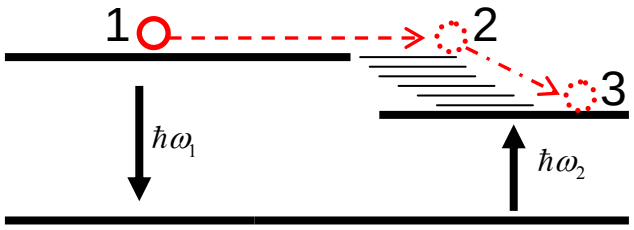

***Figure 5.3**: Two level systems assumed. Photon transition is from point 1 to the cavity and to the point 2, where it then decays to the point 3.*

CHAPTER 6: Fabrication

6.1 Fabrication of Silicon Nitride Photonic Crystals

A variety of different micro fabrication techniques (such as holographic lithography, layer-by-layer, and micromanipulation) have been used in realizing photonic crystal structures. These techniques are very application dependent and could vary based on the dielectric material used in the process. In the following we will discuss a simple technique for fabricating these structures, which takes advantage of electron beam lithography for creating very small feature sizes.

To fabricate photonic crystal cavities, cleaved pieces of wafer-type-II as discussed in Appendix A.1 are used. Then a layer of PMMA is spun coated on a piece of wafer as discussed in Appendix A.3. Patterns of photonic crystal are written using e-beam and the sample is developed in MIBK. Patterns are then transferred into the silicon nitride layer using RIE. Figures 6.1a-c are devices obtained after this process. Photonic crystal devices are then dipped into BHF to create suspended membranes. Figures 6.2a-c are some of the devices created with this technique. Some of the existing challenges in creating better-quality devices are to find a method for improving the etching process of silicon nitride. The existing mask (PMMA) does not survive the etching process and as a result membranes are thinned out and their surfaces are rough. Another point of consideration is to create more straight sidewalls by tweaking the writing dosage, etching, and developing processes. Moreover, holes created are enlarged from their expected values, so smaller holes should be written to achieve more correct size devices. These factors are under study and creating superior devices is anticipated.

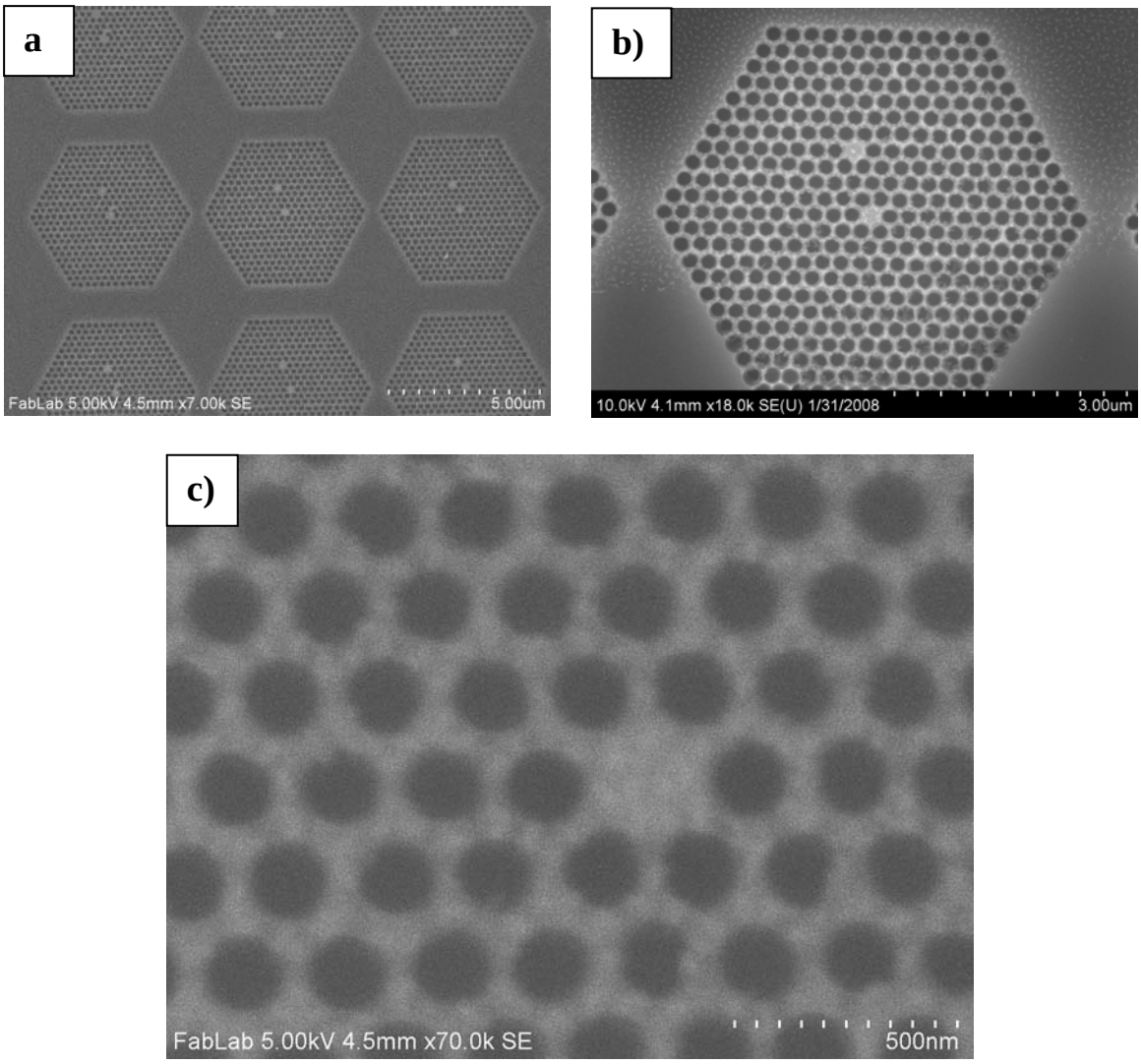

Figure 6.1: *Photonic crystal cavities after RIE process (using JEOL). Figures a-c are the images obtained from the same chip with different magnifications.*

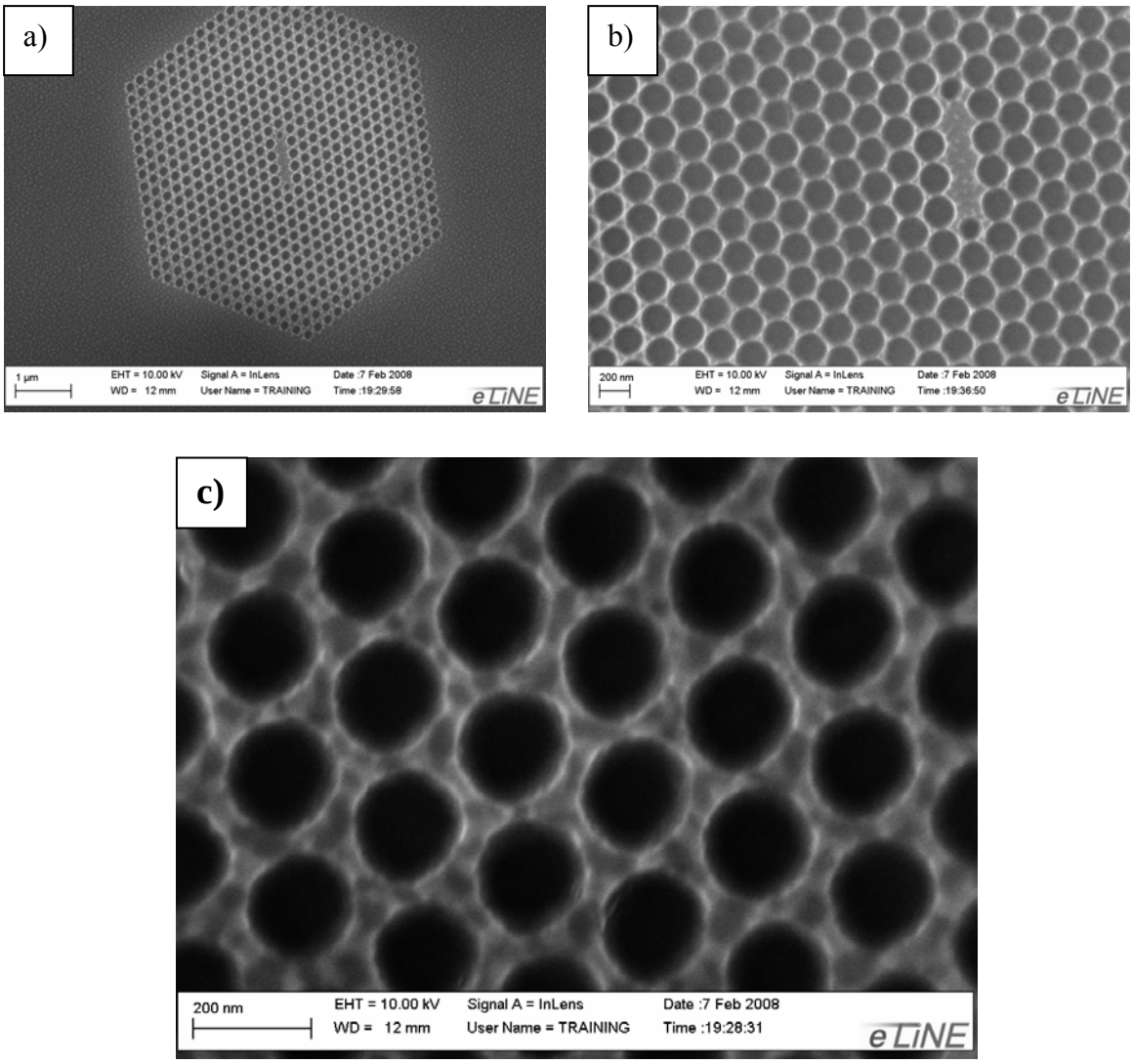

***Figure 6.2**: Patterns of photonic crystal cavities made on a slab of Silicon Nitride using Raith. Figures a-c are the images obtained from the same chip.*

6.2 Fabrication of Microdisks:

Two methods of using positive and negative photoresist have been investigated for creating Microdisks. For both approaches, cleaved pieces of wafer-type-II are used.

6.2.1 Positive Resist Approach:

A layer of PMMA is spun as indicated in Appendix A.3 on a very small piece of wafer. Patterns of negative circles are written on the sample using JEOL (e-beam Lithography). The sample is then developed in MIBK and is etched using Reactive Ion Etching (RIE), with the recipe given in Appendix A.6, for 150 seconds. The sample is dipped in Buffered HF with surfactant 6:1 for 6 minutes. Figures 6.3 a-e are some of the microdisks created with this technique. One can infer from the surfaces and the thicknesses of Silicon Nitride that the PMMA is not a robust masking layer and does not live through the RIE etching process. As shown in Figure 6.3d the thickness of the membrane is only 139nm compared to the original thickness of Silicon Nitride, which was measured to be around 270nm. Rough surfaces are also due to the RIE etching process. One way to circumvent this problem is to transfer the mask to a metallic layer such as chrome. To create the metallic mask, one can write and develop cylindrical holes in PMMA, grow a thin layer of metal, and undercut the remaining metal by removing the PMMA. This technique is under investigation. Another drawback of writing negative circles is when the e-beam fails to write some lines as shown in Figure 6.3b, and consequently, complete circles are hard to achieve.

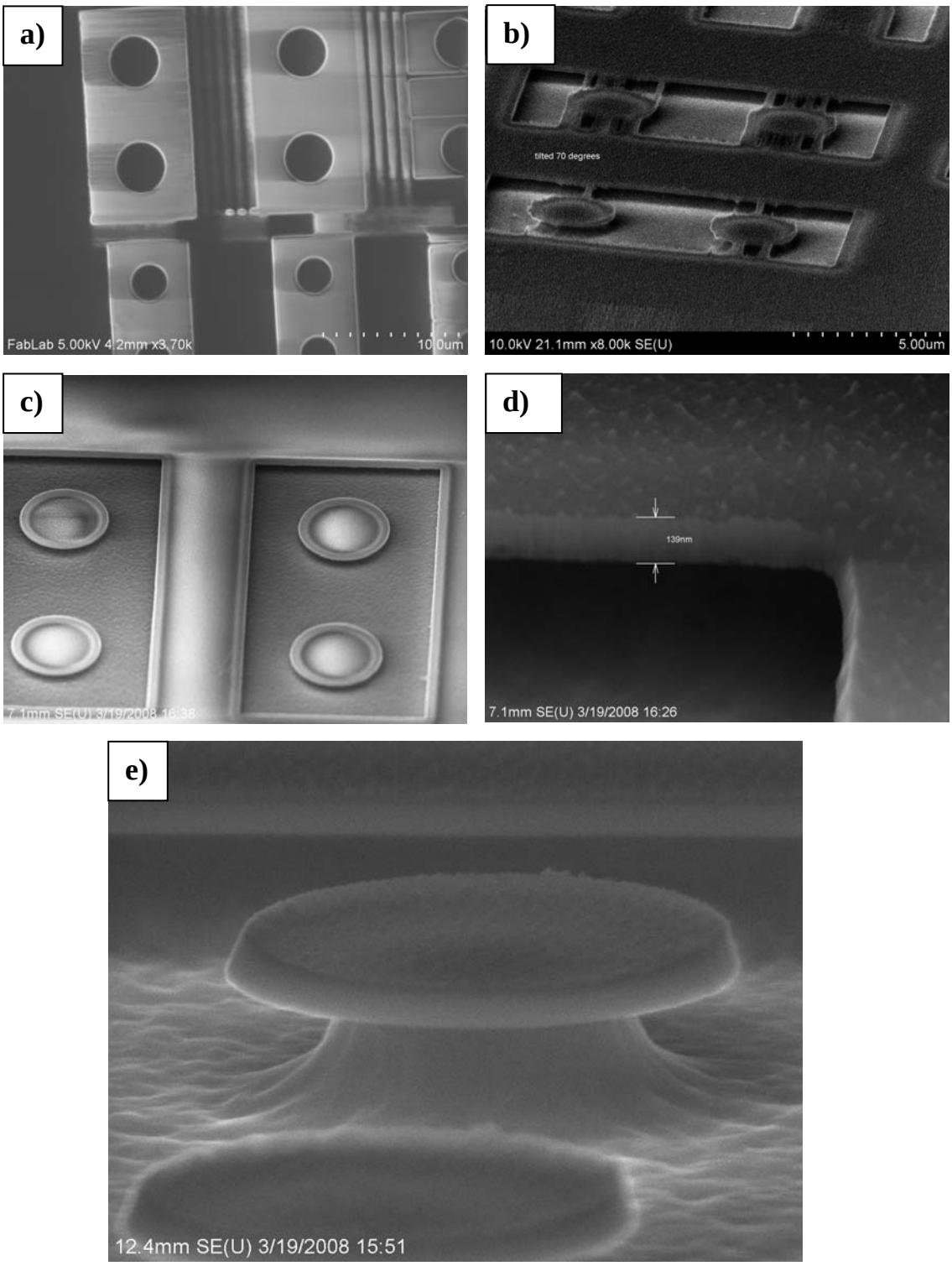

***Figure 6.3**: Microdisk resonators created using positive resist. a) SEM image after RIE etching. b) Structure with an unsuccessful write. c) SEM image of the microdisk from the top. d) To show the device thickness. e) Microdisks examined at an angle.*

6.2.2 Negative Resist Approach:

A layer of FOX-14 is spun on a piece of wafer as discussed in Appendix A.4. Circles with different radii are written using JEOL and are developed in CD-26. The sample is then etched using RIE for 150 seconds to get through the layer of Silicon Nitride (etch recipe is given in Appendix A.6). The structure obtained after this process is shown in Figure 6.5, where the resist thicknesses after RIE is measured to be about 117nm while the Silicon Nitride thickness is measured to be around 266nm. Next, the sample is dipped into the Buffered HF with surfactant 6:1 for 6 minutes to undercut the disks and to create pedestals. Initial devices lacked a clean surface and are shown in Figures 6.5 a-c. Later, beautiful microdisks with different sizes were fabricated and are shown in Figure 6.6a-f. Although these devices look very good and promise to have high-Q factors, a very thin layer of FOX seems to be present. To eliminate this problem, FOX-14 was spun at thinner thicknesses by diluting it with MIBK 1:1. Disks were written using the Raith e-beam and results indicated that the Silicon Nitride layer is getting etched. This indicates that the layer of FOX is very thin, which does not withstand the RIE process. An optimal thickness of FOX (through diluting with MIBK) that is thick enough to survive the RIE etching process and adequately thin to be etched after the undercutting process is under investigations.

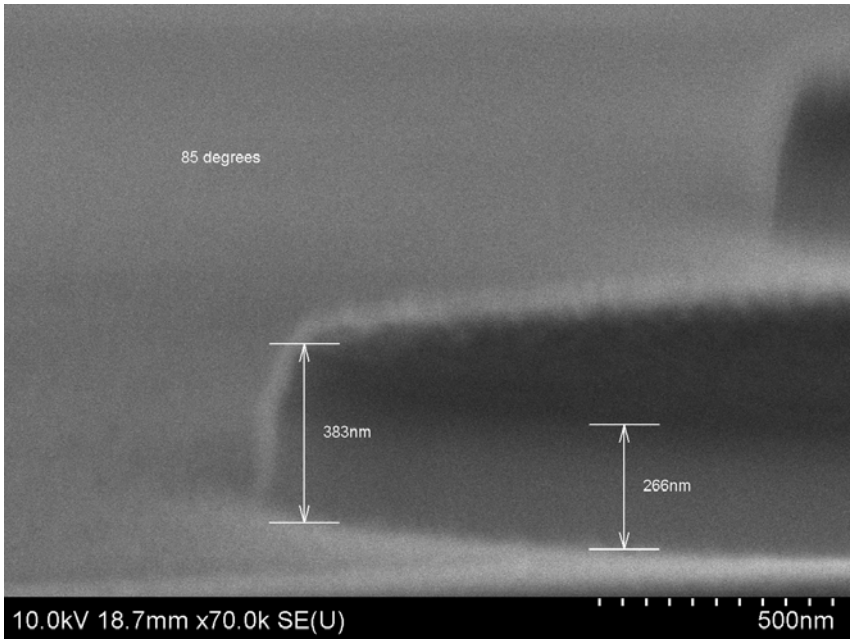

***Figure 6.4**: SEM image of FOX on silicon nitride after RIE process.*

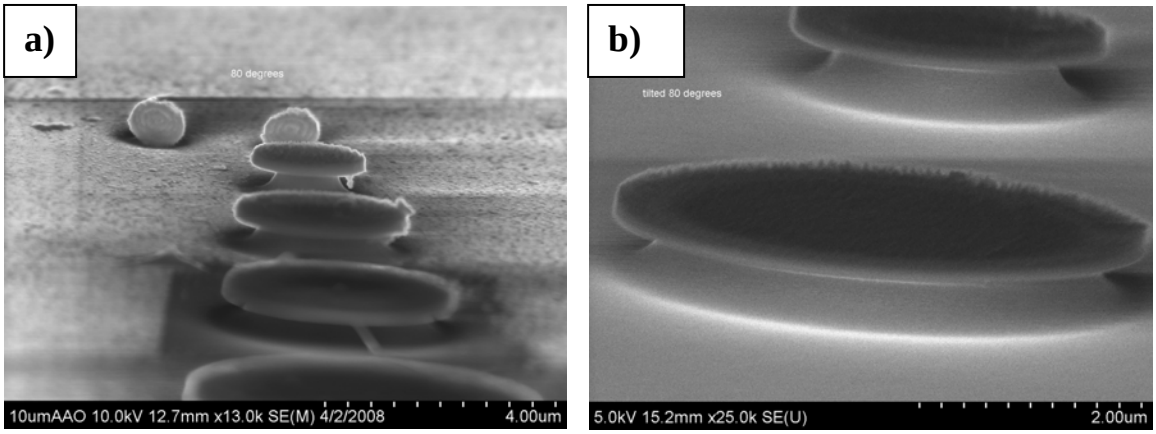

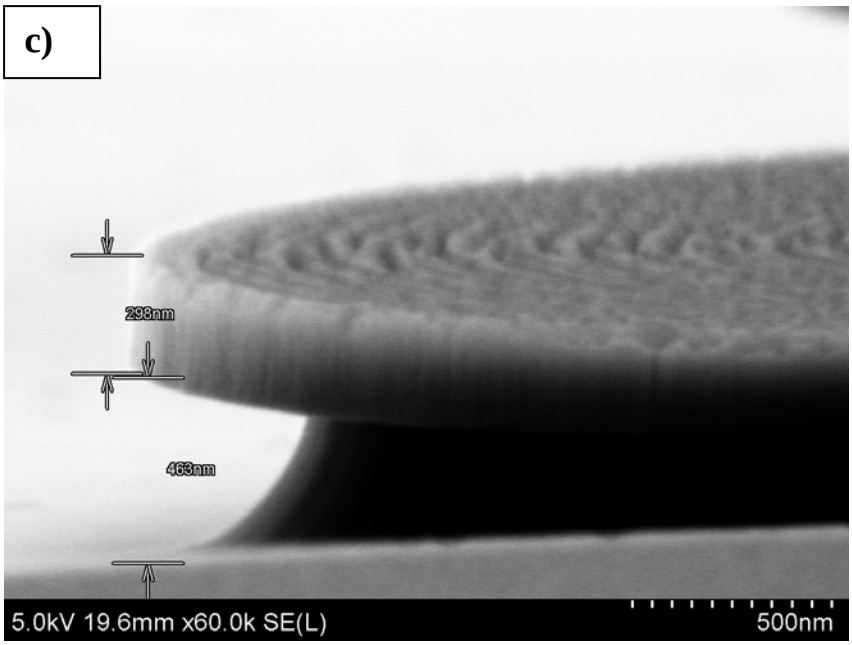

***Figure 6.5**: SEM images of microdisks with rough surfaces.*

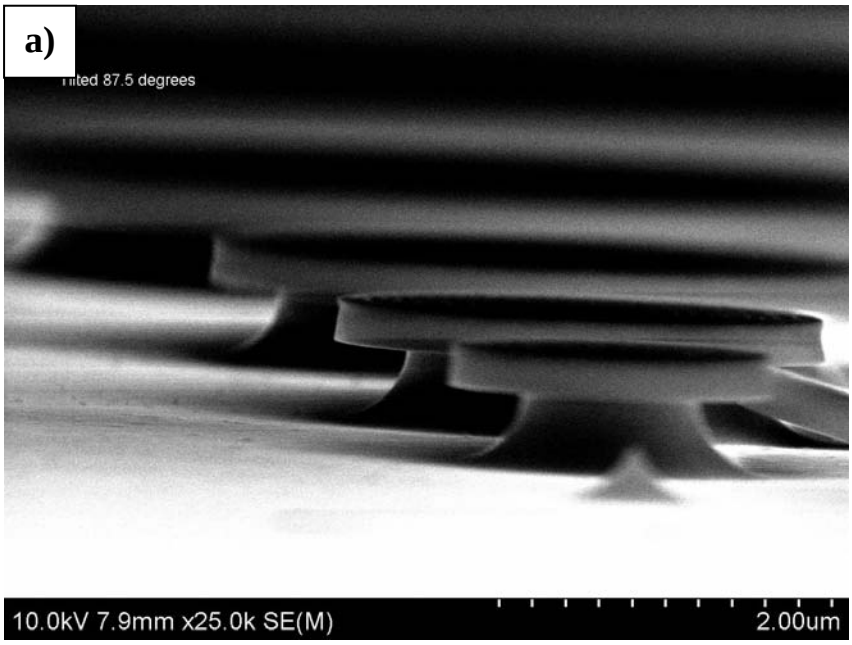

b)

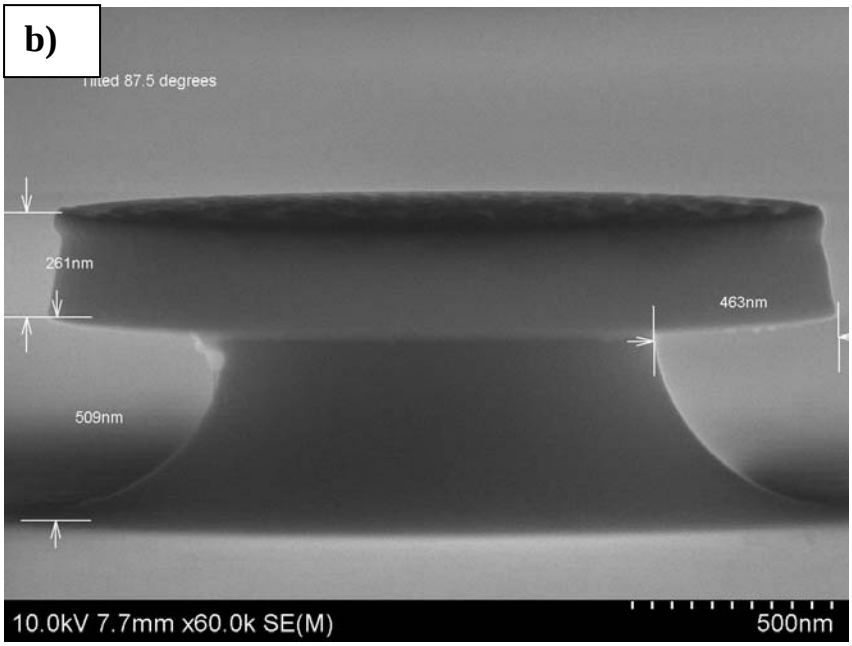
Tilted 87.5 degrees
261nm
463nm
509nm
10.0kV 7.7mm x60.0k SE(M)
500nm

c)

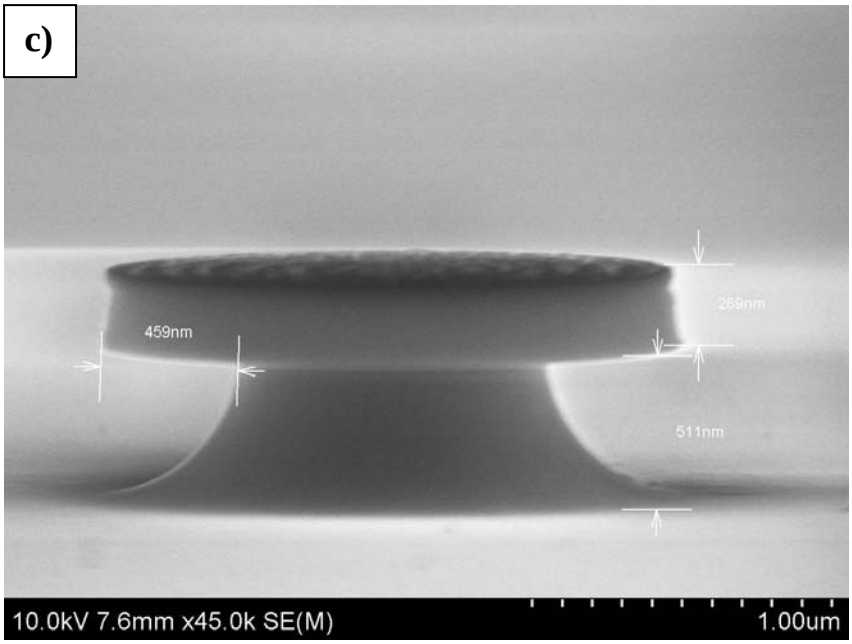
459nm
269nm
511nm
10.0kV 7.6mm x45.0k SE(M)
1.00um

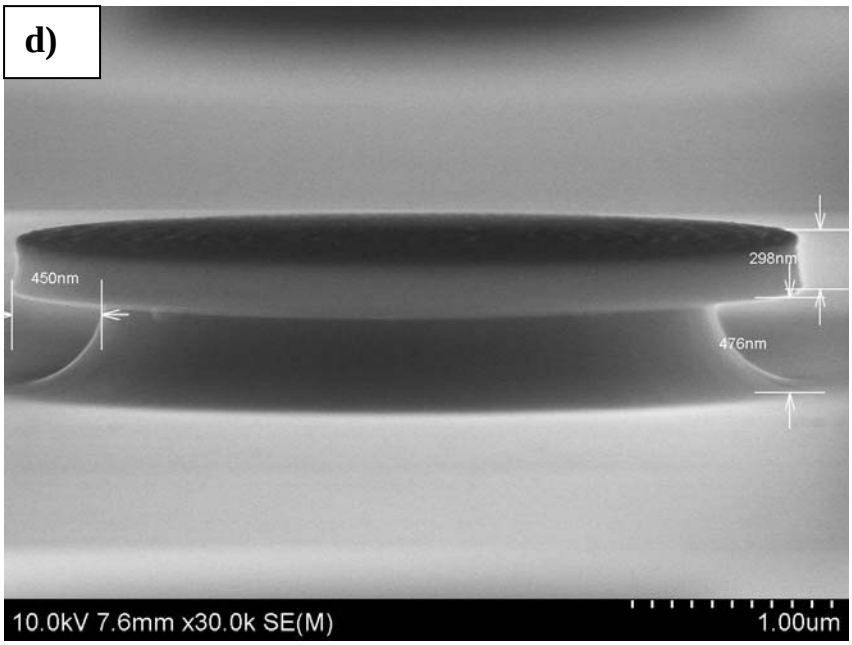
d)
298nm
450nm
476nm
10.0kV 7.6mm x30.0k SE(M)
1.00um

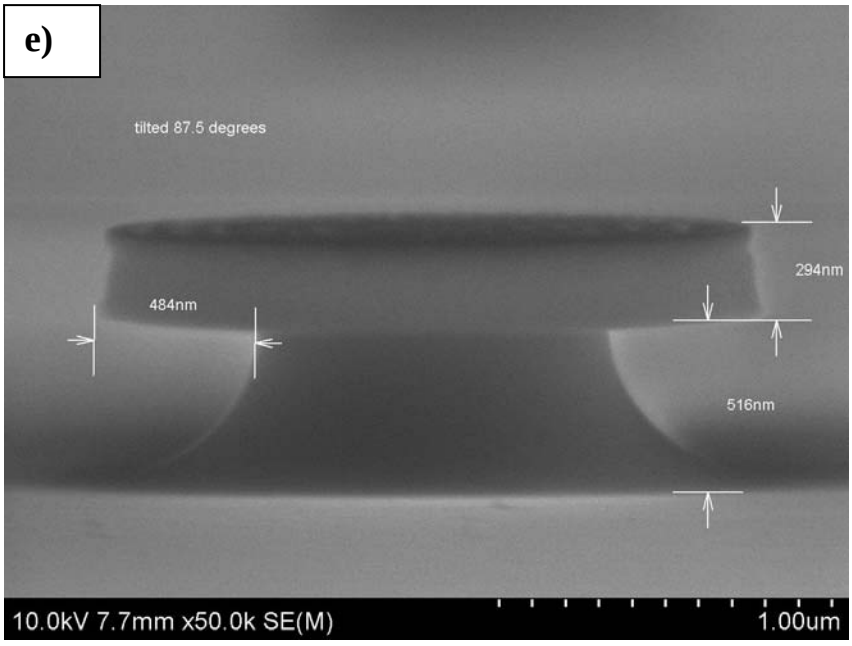
e)
tilted 87.5 degrees
294nm
484nm
516nm
10.0kV 7.7mm x50.0k SE(M)
1.00um

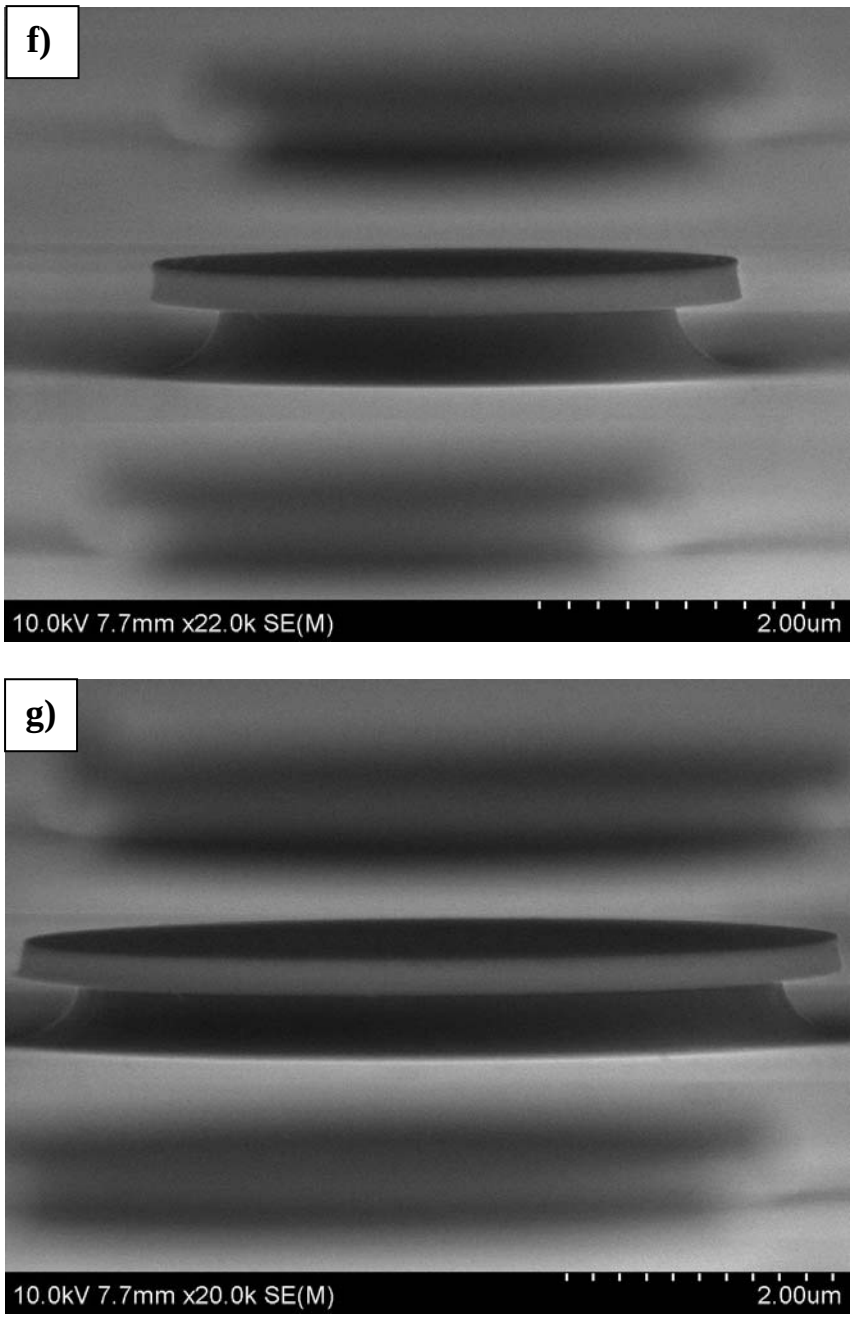

***Figure 6.6a-g**: SEM images of microdisks of different sizes.*

6.3 Silicon Nitride Membrane

Anisotropic techniques of using Deep Reactive Ion Etching and KOH have been studied for fabricating Silicon Nitride Membranes.

a) To create membrane using the DRIE technique, the following procedures are followed:

1) We start out with wafer-type-II
2) Photolithography as given in Appendix A.5, with the appropriate mask, is used to create patterns to be etched through on the back of the sample.
3) RIE is used to remove the Silicon Nitride (Appendix A.6)
4) Sample is dipped in the BHF for 12 minutes to remove the Silicon Dioxide.
5) Sample is then glued on its surface to a handling wafer (which itself has a coating of resist) using photoresist.
6) Deep holes are then created on the sample using DRIE, where Silicon Dioxide acts as an etch stop.
7) Sample is then detached from the wafer holder by dipping into Acetone.
8) BHF is used to remove the Silicon Dioxide attached to the Silicon Nitride membrane

The schematic of this process is shown in Figure 6.7a, where the actual membrane fabricated is shown in Figure 6.7b.

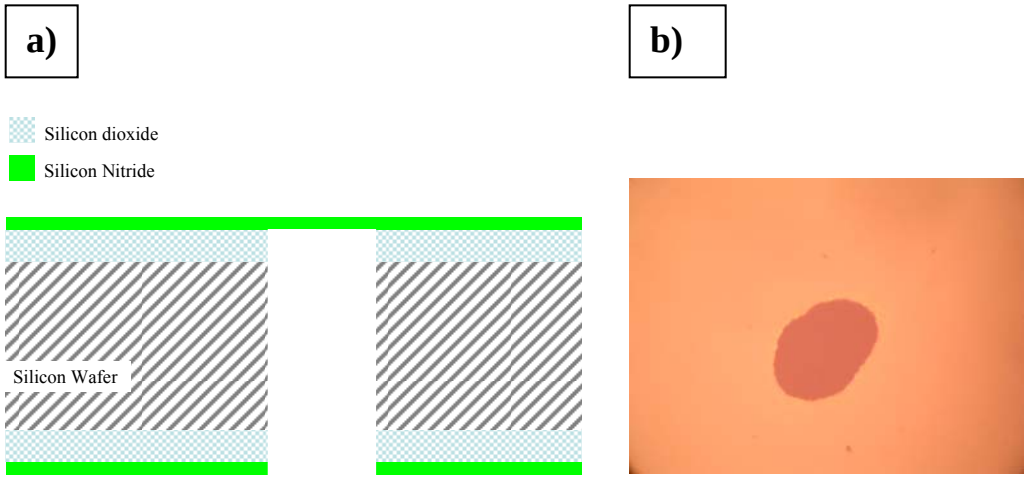

***Figure 6.7**: a) Schematic for creating silicon nitride membrane using DRIE. b) Optical microscopy of the membrane created.*

b) The following steps were taken to create Silicon Nitride membranes using KOH

1) We start out with a cleaved piece of wafer-type-I (Appendix A.1).
2) We then protect the surface by growing a very thin layer of Chrome (20nm).
3) Photolithography is then used to create patterns on the back of the sample to be etched (Appendix A.5).
4) Sample is then placed in the solution of KOH prepared as given in Appendix A.8 for few hours
5) Sample is periodically removed from the solution until the membranes are observed. Note that silicon is etched along its 111 crystal direction (57.4º) from the surface.
6) Sample is then dipped in Chrome etch for about 20 minutes.

The schematic of this process is shown in Figure 6.8a, where the actual membranes fabricated are shown in Figure 6.8b. In practice, this method is simpler and the membranes created with this method seem to have cleaner surfaces and are less stressed.

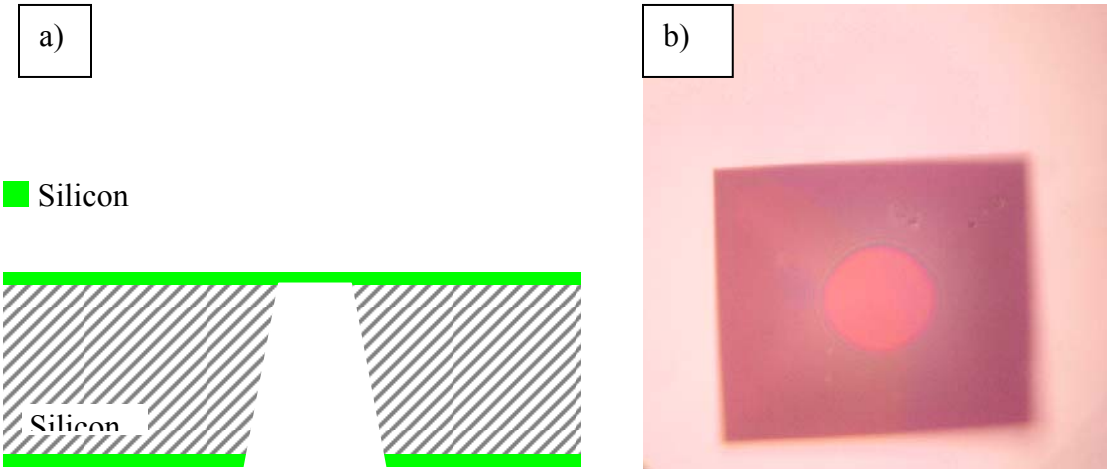

***Figure 6.8**: a) Schematic for creating silicon nitride membrane using KOH. b) Optical microscopy of the membrane created.*

6.4 Green Semiconductor Laser

The goal is to create photonic crystal cavities with embedded light sources on membrane of Silicon Nitride. This work could lead to the creation of green semiconductor laser.

1) Start out with two cleaved pieces of wafer-type-II.
2) Follow the RCA cleaning procedure [39]
3) Wafer bonding using PMMA mixed with green CdSe quantum dots as an adhesive layer. To perform this step:
    - Spin coat a layer of QDs diluted in PMMA on one of the two pieces of wafer
    - Place the second piece on the coated sample and put them on a hot plate (120°C) and exert point pressure for several minutes. Note that we did not exceed this temperature in order for the dots to be safe.
    - Slowly take the glued sample and place it in cool surroundings
    - We have obtained wafers with very strong bonding.
4) Remove SiN and SiO_2 from the top wafer using RIE
5) Use DRIE to etch away the top bulk Silicon
6) Remove SiO_2 from the surface using buffered HF
7) Create photonic crystal cavities and undercut.

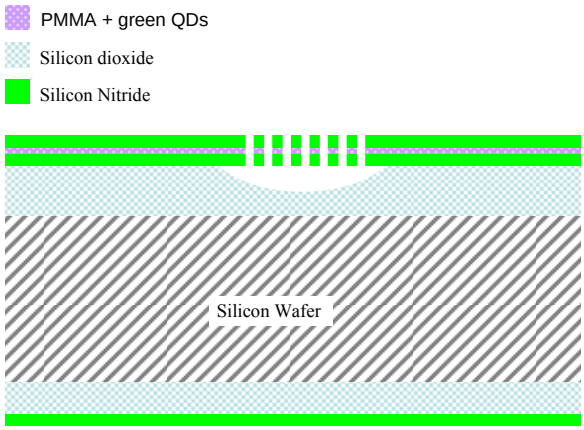

***Figure 6.9**: Schematic of the proposed green semiconductor laser*

In practice, we have followed this process-flow up to the step 6, where we obtained two layers of silicon nitride sandwiching an adhesive layer of quantum dots and PMMA, sitting on a micrometer thick oxide. Although there are places where we can create photonic crystal cavities on a suspended membrane, the structure does not contain a clean surface. We relate this problem to the point pressures exerted on the top surface for creating wafer bonding. This results in grooves on the sample, which are etched quicker and places where the etching process is very slower. To fix this problem, point pressure was replaced by a weight, but the bonding created was not strong and the top silicon nitride layer was partially peeled off after the DRIE process. Wafer bonding at temperatures of up to 180°C should be studied next and the performance of QDs after bonding should be analyzed. Another point of considerations is to use two samples of Wafer-I and to use KOH etching process or to employ colloidal QDs that survive higher temperatures and take advantage of other wafer bonding techniques.

CHAPTER 7: Conclusion and Future Work

In this thesis, we have presented the design and fabrication of photonic crystal cavities on a thin membrane of silicon nitride, with very high Q-factors and small mode volumes. In addition, we have reported for the first time the positioning of CdSe QDs on a thin membrane of silicon nitride using electroosmotic flow and have discussed our ideas for freezing QDs' kinetics through solidifying the liquid. The next step would be to merge and integrate these efforts with the goal of steering and coupling QDs to the photonic crystal cavities. This paves the way to the creation of all optical interconnects on a chip. Some of the remaining work and challenges are to refine the fabrication recipe, to perform the optical measurements, and to further improve the control algorithm for manipulating QDs. In this thesis, we have also investigated the design and fabrication of silicon nitride microdisk resonators for application in biological sensing and single photonic lasers. Meanwhile, for the purposes of single cell experiments, we have derived (all quantum mechanically) the energy transfer and the efficiency of transferring a photon between a QD donor and an acceptor modified by a single mode cavity.

Appendix A: Fabrication Recipe

A.1 Wafer-type-I:

Wafers are prepared as follows:

1. Starting out with a 4'' p-type silicon wafer <100> P-type, 2S polished, 100mm diameter, 500 +/- 20 um thick
2. Cleaning procedure
3. Growing 250nm of SiN using LPCVD (grown at NIST)

A.2 Wafer-type-II:

Wafers are prepared as follows:

1. Starting out with a 4'' p-type silicon wafer <100> P-type, 2S polished, 100mm diameter, 500 +/- 20 um thick
2. Cleaning procedure
3. Growing 1µm of SiO2 using LPCVD (grown at NIST)
4. Growing 250nm of SiN using LPCVD (grown at NIST)

Schematic in Figure A.1 is obtained.

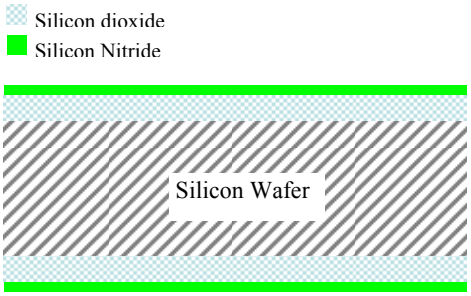

Figure A.1: *Wafer-type-II*

A.3 E-Beam Lithography Using Positive Resist:

1. Pre-bake 180ºC for 1-2min

2. Spin 950 PMMA-A4 (purchased from Microchem) at 2500rpm for 1 min to achieve a thickness of approximately 2500A based on the curve shown in Figure A.2. Thinner coating could be achieved through diluting with Anisole.
3. Post-bake at 180 ºC for 1-2min
4. Use doses in the range of 80-120 for writing anti-circles and 300-400 when writing photonic crystal cavities and trenches (JEOL 30KV).
5. Develop by dipping in MIBK/IPA (1/3) for 40s
6. Rinse with IPA for 20s
7. Rinse with DI water

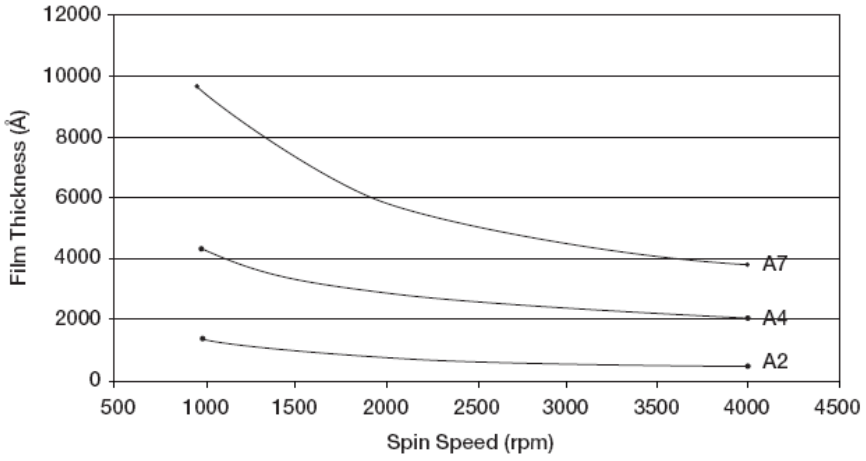

Figure A.2: *Spin curve of 950 A PMMA; 4% line (A4) is the curve we follow.*

A.4 E-Beam Lithography Using Negative Resist:

1. Pre-bake at 180ºC for 1-2min
2. Place FOX14 in room temperature 1hr prior to use, do not shake the bottle, and take liquid from the middle and not from the surface or the bottom.

Note: more information about FoX-14 could be found at:

http://www.dowcorning.com/applications/search/default.aspx?R=655EN

3. Spin flowable oxide (FoX-14) MIBK at 3000rpm for 1 min, you may achieve thinner coating by diluting FoX with MIBK
4. Post-bake 90ºC for 3min
5. Recommended doze for e-beam (JEOL at 30KV): 450-550
6. Develop in CD-26 for 8 min
7. Rinse with DI water

Some Characteristics of FOX-14 are as follows:

- Flowable oxide (FoX-14) has an index of 1.443 at 250nm thickness (measured using an ellipsometer).
- FoX could be etched away using HF.
- It is a more robust mask when compared to PMMA while etched in RIE.
- It is not possible to create contamination dots using e-beam, and thus, gold nano-particles should be used for focusing and stigmation.

A.5 Photolithography

1. Pre-bake for two minutes on a hot plate
2. Adjust the sample on the spinner and place a drop of HDMS primer on it
3. Place a drop of 1813-shipley and spin for 40s at 4000rpm
4. Post bake at 90°C for 1min
5. Expose to UV for 9 seconds
6. Develop at 352-developer for 40s
7. hard bake for 1 min

After this process, 1.4μm thick resist is obtained.

A.6 Reactive Ion Etching (Trion machine)

The best etch recipe experimented so far is:

RF=70W; P=50mtorr; SF_6=30sccm; O_2=1sccm

For PECVD Silicon Nitride the results are summarized in table A1.

Table A1: Etch rate PECVD

TIME (second)	2	20	30	40	**Etch Rate (A/10s)**
SiN	474	-	1450	1993	485.2
Si+PMMA	411	967	1580	2170	490.9
Si	1890	4137	6512	8670	2074

LPCVD Silicon Nitride are used with the recipe of RF=70W, P=20mtorr, SF_6=30sccm, and O_2=0sccm, and the etch rates are given in table A2.

Table A2: Etch rate LPCVD

TIME (second)	20	30	40	60	**Etch Rate (A/10s)**
SiN	373	771	977	1144	209
Si+PMMA	916	1771	2548	4685	553

The result for a different etching process used mainly in this project (RF=70W; P=50mtorr; SF_6=30sccm; O_2=1sccm) is given in table A3.

Table A3: Etch rate LPCVD

TIME (second)	30	60	90	120	**Etch Rate (A/10s)**
SiN	550	1237	1982	2181	197
Si+PMMA	930	2300	2610	3286	327

Note: We find Trion to be a very unstable machine and the results usually vary from one process to another.

A.7 Index and thickness measurement of Silicon Nitride

Knowing the index of refraction in our wafers is very crucial for performing simulation. Therefore, measurements were taken using N&K analyzer, ellipsometry technique, to

find the index of refraction as shown in Figure A.3. Meanwhile, the thickness of Silicon Nitride was measure to be 278nm.

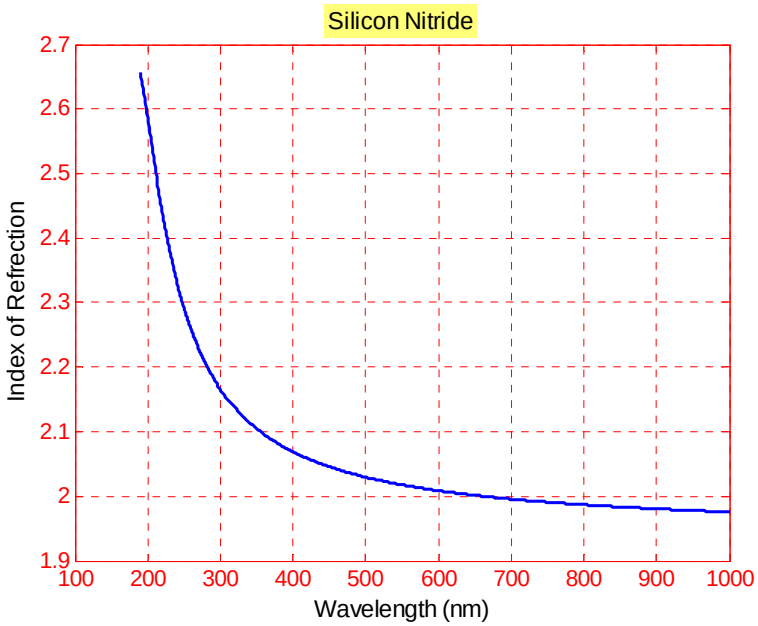

Figure A.3: *Index of refraction of LPCVD silicon nitride measured using ellipsometry technique.*

A.8 KOH Etching of Bulk Silicon

Silicon Nitride or Silicon Dioxide are used as a masking layer for etching the bulk Silicon, while the patterns are created using optical lithography in conjunction with RIE. Silicon is etched in its <111> crystal directions. For our wafers that have surfaces of <100> direction, etching occurs at an angle of 54.74°. KOH solution and etching setup could be prepared as follows [40]:

1. Mix 30% Potassium Hydroxide (KOH) by weight to 450ml DI water (135 grams of KOH)
2. Set the probe temperature at 85°C by placing the beaker on a hot plate
3. Place a magnet in the beaker and set it to spin at 220rpm

4. Dip the sample in the solution in a way that it does not perturb the spinning magnet

5. Place a lid on the solution to prevent evaporation

Etch rate of 1.4 um/min is observed. This rate is also reported in [etch rate]. A thin metallic layer could be used to keep the surfaces clean and unaffected by the solution.

Appendix B: Simulation

B.1 CODE FOR MPB SIMULATION:

```
; This program simulates a triangular lattice

(define-param h .74)
(define-param r 0.25)
(define-param supercell-h 4)
(define-param eps 4.4521)
(define-param loweps 1)

(define diel (make dielectric (epsilon eps)))

(set! num-bands 8)
(set! geometry-lattice (make lattice(size 1 1 supercell-h)
                                    (basis1 (/ (sqrt 3) 2) 0.5)
                                    (basis2 (/ (sqrt 3) 2) -0.5)))

;(define-param sd (list 0 1))
;(set! sd (interpolate 5 sd))

(set! geometry (list

                (make block
                (center 0 0 0)(size 1 1 supercell-h)
                (material (make dielectric(epsilon loweps))))

                (make block
                (center 0 0 0)(size 1 1 h)
                (material (make dielectric(epsilon eps))))

                (make cylinder
                (center 0 0 0) (radius r) (height supercell-h)
                (axis 0 0 1)
                (material air))))

(define Gamma (vector3 0 0 0))
```

```
(define M (vector3 0 0.5 0))
(define K (vector3 (/ -3)(/ 3) 0))
(define Kreq (vector3 0 0.2 0))

(set! k-points (list Gamma            ; Gamma
                     M                                    ; M
                     K                                    ; K
                     Gamma))                ; Gamma

;(set! k-points (list          ; Gamma
 ;              M              ; M
  ;             K              ; K
   ;            ))         ; Gamma
 ;

(set! k-points (interpolate 4 k-points))

(set! resolution 32)

(run-tm)
(run-te)
;(run-te (output-at-kpoint (vector3 0 0.5 0)
   ;  (vector3 (/ -3)(/ 3) 0)
   ;  fix-efield-phase output-efield-z))
;(run-zeven  fix-efield-phase output-hfield-z)
;(run-tm (output-at-kpoint (vector3 0 0.5 0)(vector3 (/-3)(/ 3) 0) fix-hfield-phase output-h;field))
```

B.2 MEEP SIMULATION

```
; Photonic crystal slab consisting of a triangular lattice of air
; holes in a finite-thickness dielectric slab, optionally with a
; substrate on one side of the slab.  See the paper: S. G. Johnson,
; S. Fan, P. R. Villeneuve, J. D. Joannopoulos, L. A. Kolodziejski,
; "Guided modes in photonic crystal slabs," PRB 60, 5751 (August
; 1999).

; Note that this structure has mirror symmetry throught the z=0 plane,
; and we are looking at k-vectors in the xy plane only.  Thus, we can
; break up the modes into even and odd (analogous to TE and TM), using
; the run-zeven and run-zodd functions.

(define-param h 0.74) ; the thickness of the slab
(define-param eps 4.4521) ; the dielectric constant of the slab
(define-param loweps 1.0) ; the dielectric constant of the substrate
(define-param r 0.26) ; the radius of the holes
(define-param r2 0.14) ; the radius of the defect holes
```

```
(define-param supercell-h 4) ; height of the supercell
(define-param size_x 20)
(define-param size_y 20)
(define-param dpml 1)

; triangular lattice with vertical supercell:
(set! geometry-lattice (make lattice (size (+ size_x dpml) (+ size_y dpml)  supercell-h)
                    (basis1 (/ (sqrt 3) 2) 0.5)
                    (basis2 (/ (sqrt 3) 2) -0.5)))

; makes the membrane without holes
(set! geometry
     (list (make block (material air)
                                          (center 0 0 0)
                                          (size infinity infinity supercell-h))
                         (make block (material (make dielectric (epsilon eps)))
                                          (center 0) (size infinity infinity h))))

(define center_x 0)
(define center_y 0)

; makes the finitely large photonic crystal by appending the holes
(do ((x -20 (+ x 1))) ((> x 20))
                    (do ((y -20 (+ y 1))) ((> y 20))
                    (set! center_x (* (+ x y) (/ (sqrt 3) 2)))
                    (set! center_y (* (- x y) 0.5))
                    (if (and (< (abs center_x) (abs (- (/ size_x 2) r))) (< (abs center_y) (abs (- (/ size_y 2) r))))
                    (set! geometry (append geometry (list (make cylinder (material air) (center center_x
                    center_y) (radius r) (height supercell-h)))))
                    )
      )
)

; takes out the three holes to make the cavity
(do ((y -2 (+ y 1)))((> y 2))
(set! geometry (append geometry
                  (list (make cylinder (center 0 y)
                           (radius r) (height h)
                          (material (make dielectric (epsilon eps))))))))

; replace the two voids with holes of smaller radii
(define-param d (+ 2 (- r r2)))
(set! geometry (append geometry
                                                    (list      (make cylinder (center 0 d)
                                                               (radius r2) (height h) (material air))
                                                               (make cylinder (center 0 (* -1 d))
                                                               (radius r2) (height h) (material air)))))
```

```
;(run-until 1 (at-beginning output-epsilon))
;(run-sources+ 200
;             (at-beginning output-epsilon))

(define-param fcen 0.388146) ;pulse center frequency
(define-param df 0.1) ; pulse width (in frequency)
;(define-param fcen 0.249) ; pulse center frequency
;(define-param df 0.1)    ; pulse width (in frequency)

(set! sources (list
              (make source
                (src (make gaussian-src (frequency fcen) (fwidth df)))
                (component Ex)
                (center 0 0))))

(set! symmetries (list (make mirror-sym (direction Z)) (make mirror-sym (direction X) (phase -1))
                       (make mirror-sym (direction Y))))
(set! pml-layers (list (make pml (thickness 1.0))))
(set-param! resolution 20)
(run-sources+ 200
             (at-beginning output-epsilon)
             (after-sources (harminv Ex (vector3 0 0) fcen df)))

;(run-until (/ 1 fcen) (at-every (/ 1 fcen 20) output-hfield-z))
(run-until (/ 1 fcen) (at-every (/ 1 fcen 20) output-efield))
```

MEEP OUTPUT (HARMINV):

h=0.74 r=0.26 r2=0.14 fcen=0.388146 df=0.01 +200 20*20						
harminv0:	frequency	imag. freq.	Q	|amp|	amplitude	error
harminv0:	**0.388**	-5.82E-05	**3335.7894**	6.526811	-6.03122973050731-2.49470022888955i	1.07E-11
h=0.74 r=0.25 r2=.12 fcen=0.385339 df=0.02 + 100						
harminv0:	frequency	imag. freq.	Q	|amp|	amplitude	error
harminv0:	0.377	-8.86E-04	212.62483	2.42E-04	1.09890075037321e-4+2.15450250821265e-4i	2.49E-05
harminv0:	**0.385**	-5.33E-05	**3617.4462**	3.3645536	1.5256072900567-2.99879026707197i	3.31E-10

B.4 MATLAB CODE FOR MODE VOLUME:

```
% This code calculates the modevolume and illustrates how the field changes
% at distances above and below the center of the cavity
clear all
close all
% ******************************
```

```
% Plotting the eps with z-cross section at the center of the PC
datadenergy=hdf5read('R24-3holedefect-denergy-000304.92','/denergy');
dataeps=hdf5read('R24-3holedefect-eps-000000.00.h5','/eps');
for n1=1:1:96
    veceps(n1)=dataeps(n1,252,252);
end
plot([0:1:95],sqrt(veceps),'*');grid
xlabel('Data Points')
ylabel('Index of Refraction')
pause(10)
% ******************************
A=0;
for n=1:1:96
    V=abs(datadenergy(n,252,252));
    A(n)=V; %Electric field energy in the z-direction
end
Mid=abs(datadenergy(48,252,252)); %Maximum Electric Field Energy along the
B=A./Mid;
plot([0:1:95],B.*(veceps./dataeps(48,252,252)).^-.5,'r');grid
xlabel('Data Points')
ylabel('Electric field energy over its maximum')
% Calculating ModeVolume
ff=0;
for nx=1:1:504
    for ny=1:1:504
        for nz=1:1:96
            f=abs(datadenergy(nz,nx,ny));
            ff=f+ff; %Total Electric Energy
        end
    end
end
M=ff/Mid;
Res=24; %Resolution of the simulation
E=M/Res^3;
% To find E/((lamda/n)^3)
w=0.38842;
index=sqrt(dataeps(48,252,252)); %Index at the center
ModeVolume = E*((w*index)^3)
```

B.5 MICRODISKS MEEP SIMULATION (2D):

; Calculating 2d ring-resonator modes, from the Meep tutorial.

```
(define-param n 2.2) ; index of waveguide
(define-param w .65) ; width of waveguide
(define-param r .7) ; inner radius of ring

(define-param pad 4) ; padding between waveguide and edge of PML
(define-param dpml 2) ; thickness of PML

(define sxy (* 2 (+ r w pad dpml))) ; cell size

(set! geometry-lattice (make lattice (size sxy sxy no-size)))

; Create a ring waveguide by two overlapping cylinders - later objects
; take precedence over earlier objects, so we put the outer cylinder first.
; and the inner (air) cylinder second.
(set! geometry (list
                                    (make cylinder (center 0 0) (height infinity)
                                        (radius (+ r w)) (material (make dielectric (index n))))
                    ))
;                   (make cylinder (center 0 0) (height infinity)
                    ;                       (radius r) (material air))))

(set! pml-layers (list (make pml (thickness dpml))))
(set-param! resolution 46)

; If we don't want to excite a specific mode symmetry, we can just
; put a single point source at some arbitrary place, pointing in some
; arbitrary direction.  We will only look for TM modes (E out of the plane).

(define-param fcen 1.5) ; pulse center frequency
(define-param df 0.3)  ; pulse width (in frequency)
(set! sources (list
            (make source
              (src (make gaussian-src (frequency fcen) (fwidth df)))
              (component Ex) (center (+ r w) 0))))

; exploit the mirror symmetry in structure+source:
(set! symmetries (list (make mirror-sym (direction Y))))

(run-sources+ 200
                        (at-beginning output-epsilon)
                        (after-sources (harminv Ex (vector3 (+ r w)) fcen df)))

; Output fields for one period at the end.  (If we output
; at a single time, we might accidentally catch the Ez field when it is
; almost zero and get a distorted view.)
(run-until (/ 1 fcen) (at-every (/ 1 fcen 20) output-hfield-z))
```

OUTPUT (HARMINV):

r=1 fcen=1.5 df=0.3						
harminv0:	frequency	imag. freq.	Q	|amp|	amplitude	error
harminv0:	1.367	-0.002944	232.22861	0.0028213	-3.42670334635615e-4-0.00280038202909005i	1.45E-05
harminv0:	**1.415**	-3.21E-05	**22026.587**	**0.031908**	0.028854274677386 9-0.0136218111525341i	1.72E-06
harminv0:	1.454	-0.001712	424.66916	0.118003	-0.0210636890166924+0.116107785299177i	1.02E-06
harminv0:	**1.493**	-3.86E-06	**193138.92**	**0.1625484**	-0.112629652232747-0.117203033703086i	7.44E-08
harminv0:	1.54	-9.24E-04	833.52239	0.1426695	0.106262658244144+0.0951989643208133i	3.44E-07
harminv0:	1.546	0.010753	-71.8806	4.36E-04	-2.38679965725251e-4-3.65009282895904e-4i	0.002758
harminv0:	**1.57**	-5.53E-06	**141879.51**	**0.0606214**	-0.031262788250077 8+0.0519383529356594i	2.00E-06
harminv0:	1.624	-4.01E-04	2022.8658	0.006647	-0.0063137145966602 8+0.00207842137771464i	2.02E-06
harminv0:	1.648	-4.86E-05	16967.207	0.0016915	0.0016052768984788 3+5.33174980729994e-4i	3.03E-06

B.6 MICRODISKS MEEP SIMULATION (3D):

```
; Calculating 3d ring-resonator modes, from the Meep tutorial.

(define-param n 2.2) ; index of waveguide
(define-param w 0.5) ; width of waveguide
(define-param r 0.5) ; inner radius of ring
(define-param h 0.3) ; the thickness of the slab
(define-param supercell-h 4) ; height of the supercell

(define-param pad 4) ; padding between waveguide and edge of PML
(define-param dpml 2) ; thickness of PML

(define sxy (* 2 (+ r w pad dpml))) ; cell size

(set! geometry-lattice (make lattice (size sxy sxy supercell-h)))

; Create a ring waveguide by two overlapping cylinders - later objects
; take precedence over earlier objects, so we put the outer cylinder first.
; and the inner (air) cylinder second.
(set! geometry (list
                                (make cylinder (center 0 0) (height h)
                                    (radius (+ r w)) (material (make dielectric (index n))))
                ))
;               (make cylinder (center 0 0) (height infinity)
                ;                   (radius r) (material air))))

(set! pml-layers (list (make pml (thickness dpml))))
(set-param! resolution 32)

; If we don't want to excite a specific mode symmetry, we can just
; put a single point source at some arbitrary place, pointing in some
; arbitrary direction.  We will only look for TM modes (E out of the plane).

(define-param fcen 1.5) ; pulse center frequency
```

```
(define-param df 0.2)  ; pulse width (in frequency)
(set! sources (list
            (make source
              (src (make gaussian-src (frequency fcen) (fwidth df)))
              (component Ex) (center (+ r w) 0))))

; exploit the mirror symmetry in structure+source:
(set! symmetries (list (make mirror-sym (direction Y))))

(run-sources+ 200
                        (at-beginning output-epsilon)
                        (after-sources (harminv Ex (vector3 (+ r w)) fcen df)))

; Output fields for one period at the end.  (If we output
; at a single time, we might accidentally catch the Ez field when it is
; almost zero and get a distorted view.)
(run-until (/ 1 fcen) (at-every (/ 1 fcen 20) output-hfield-z))
```

References

[1] E. Waks and J. Vuckovic, "Dipole Induced Transparency in Drop-Filter Cavity-Waveguide Systems", *Phys. Rev. Lett.*, Vol. 96, 153601, 2006

[2] D. Sridharan and E. Waks, "Generating entanglement between quantum dots with different resonant frequencies based on Dipole Induced Transparency", *quant-ph.* Archive: 0703089, Submitted: March 2007.

[3] K. E. Sapsford, T. Pons, I. L. Medintz, and H. Mattoussi, "Biosensing with Luminescent Semiconductor Quantum Dots", *Sensors*, Vol. 6, 925-953, 2006

[4] T. Pons, I. L. Medintz, M. Sykora, and H. Mattoussi, "Spectrally resolved energy transfer using quantum dot donors: Ensemble and single-molecule photoluminescence studies" *Phys. Rev. B*, Vol. 73, 245302, 2006.

[5] S. F. Wuister, C. D. M. Donega, and A. Meijerink, "Local-field effects on the spontaneous emission rate of CdTe and CdSe quantum dots in dielectric media", *J. Chem. Phys.*, Vol. 121, No. 9, September 2004.

[6] L. Pang, K. Tetz, Y. Shen, C. Chen, and Y. Fainman, "Photosensitive quantum dot composites and their application in optical structures", *J. Vac. Sci. Technol. B.*, Vol. 23(6). November 2006.

[7] Y. Shen, L. Pang, Y. Fainman, M. Griswold, S. Yang, L. V. Butov, and L. J. Sham, "Photoluminescence spectral switching of single CdSe/ZnS colloidal nanocrystals in PMMA", Amer. Phys. Soc., Vol. 76(8), 2007.

[8] E. Yablonovitch, "Photonic Crystals: What's in a Name?" *Optics, pp. 12-13,* March (2007).

[9] L. Rayleigh, "On the maintenance of vibrations by forces of double frequency, and on the propagation of waves through a medium endowed with a periodic structure", *Phil. mag.,* **24**, 145-159 (1887).

[10] P. Lodahl, A. F. Van Driel, I. S. Nikolaev, A. Irman, K. Overgaag, D. Vanmaekelbergh, and W. L. Vos, "Controlling the dynamics of spontaneous emission from quantum dots by photonic crystals", *Nature*, **430**, pp. 654-7 August (2004).

[11] J. P. Reithmaier, G. Sek, A. Loffler, C. Hofmann, S. Kuhn, S. Reitzenstein, L. V. Keldysh, V. D. Kulakovskil, T. L. Reinecke, and A. Forchel, "Strong coupling in a single quantum dot-semiconductor microcavity system", *Lett. Nature*, Vol. 432, No. 11, November 2004.

[12] D. Englund, A. Faraon, B. Zhang, Y. Yamamoto, and J. Vuchovic, "Generation and transfer of single photons on a photonic crystal chip", Opt. Exp., Vol. 15, No. 9, 2007.

[13] K. Sakoda, “Optical Properties of Photonic Crystals", Springer-Verlag Berlin Heidelberg (2001).

[14] J. D. Joannopoulos, R. D. Meade, J. N. Winn, “Photonic Crystals: modeling the flow of light”, Princeton University Press (1995).

[15] R. D. Meade, K. D. Brommer, A. M. Rappe, and J. D. Joannopulos, “Existence of a photonic bandgap in two dimensions”, *App. Phys. Lett.* **61**, 495 (1992).

[16] O. Painter, J. Vuchovic, and A. Scherer, “Defect modes of a two-dimensional photonic crystal in an optically thin dielectric slab”, *J. Opt. Soc.,* Vol. 16, No. 2. February 1999.

[17] M. Loncar, T. Doll, J. Vuckovic, and A. Scherer, “Design and Fabrication of Silicon Photonic Crystal Optical Waveguides”, *J. of Lightwave Tech.* **18**, No. 10, pp. 1402-12 October (2000).

[18] K. J. Vahala, “Optical Microcavities”, *Nature*, **424,** pp. 839-846, August (2003).

[19] T. Asano, B. S. Song, and S. Noda. “Analysis of the experimental Q factors (~ 1 million) of photonic crystal nanocavities”, Opt. Exp. **14**, Issue. 5, pp.1996-2002 (2006).

[20] M. Makarova, J. Vuckovic, H. Sanda, and Y. Nishi, “Silicon-based photonic crystal nanocavity light emitters”, App. Phys. Lett. Vol. 89, 221101, November 2006.

[21] M. Barth, J. Kouba, J. Stingl, B. Löchel, and O. Benson, “Modification of visible spontaneous emission with silicon nitride photonic crystal nanocavities”, Optics Express, Vol. 15, No. 25, 17231, December 2007

[22] M. Borselli, T. J. Johnson, and O. Painter, “Beyond the Rayleigh scattering limit in high-Q silicon microdisks: theory and experiment” Optics Express, Vol. 13, No. 5, 1515 February 2005.

[23] P. E. Barclay, K. Srinivasan, O. Painter, B. Lev, and H. Mabuchi, “Integration of fiber-coupled high-Q SiN microdisks with atom chips”, *Appl. Phys. Lett.*, Vol. 89, 131108, September 2006.

[24] D. G. Grler, “A revolution in optical manipulation”, *Nature*, VOl. 424, No. 14, August 2003.

[25] S. Chaudhary, and B. Shapiro, “Arbitrary Steering of Multiple Particles Independently in an Electro-Osmotically Driven Microfluidic Systems”, *IEEE Trans. Cont. Sys. Technol*., Vol. 14, No. 4, July 2006

[26] M. Armani, S. Chaudhary, R. Probst, and B. Shapiro, “Using Feedback Control of MicroFlows to Independently Steer Multiple Particles”, *J. MEMS*, Vol. 15, No. 4, August 2006

[27] J. S. Guasto, P. Huang, and K. S. Breuer, "Statistical particle tracking velocimetry using molecular and quantum dot tracer particles", *Exp Fluids*, Vol. 41, 869-880, September 2006.

[28] N. Bao, J. Xu, Q. Zhang, J. Hang, and H. Chen, "Electroosmotic flow in poly(dimethylsiloxane) microchannels", *J. Chromatography A.*, Vol. 1099, 203-206, November 2005.

[29] R. J. Yang, L. M. Fu, and Y. C. Lin, "Electroosmotic Flow in Microchannels", *J. Colloid & Interface Sci.*, Vol. 239, No. 1, 90-105, July 2001.

[30] N. T. Nguyen and S. T. Wereley, "Fundamentals and applications of Microfluidics", Norwood, MA : Artech House, 2002.

[31] L. Coolen, X. Brokmann, P. Spinicelli, and J. –P. Hermier, "Emission Characterization of a Single CdSe-ZnS Nanocrystal with High Temporal and Spectral Resolution by Photon-Correlation Fourier Spectroscopy", *Phys. Rev. Lett.*, Vol. 100, 027403-1, 2008.

[32] Kumar, R.; Raghavan S.R., Photogelling Fluids Based on Light-Activated Growth of Zwitterionic Wormlike Micelles. *J. Amer. Chem. Soc.,* 2008 (submitted)

[33] D. L. Andrews and A. A. Demidov, "Resonance Energy Transfer", John Wiley & Sons Ltd, 1999, ISBN 0 471 98732 8.

[34] G. Agarwal, and S. D. Gupta, "Microcavity-induced modification of the dipole-dipole interaction", *Phys. Rev. A.,* Vol. 667, No. 4, January 1998.

[35] A. R. Clapp, I. L. Medintz, and H. Mattoussi, "Forster Resonance Energy Transfer Investigations Using Quantum-Dot Fluorophores", *ChemPhysChem*, Vol. 7, 47-57, 2006.

[36] L. Guo, T. D. Krauss, C. B. Poitras, M. Lipson, X. Teng, and H. Yang, "Energy transfer between colloidal semiconductor nanocrystals in an optical microcavity", *Appl. Phys. Lett.*,Vol 89, 061104, 2006.

[37] J. J. Sakurai, "Modern Quantum Mechanics", 1994, ISBN 0 201 53929 2.

[38] J. W. Norbury and P. A. Deutchman, "Resonance formation and decay: An application of second-order, time-dependent perturbation theory", *Am. J. Phys.*, Vol. 52, No. 1, January 1984.

[39] S. Wolf and R. N. Tauber, Silicon Processing for the VLSI Era, Vol. 1: Process Technology. Sunset Beach, CA, USA: lattice Press, Second ed., 2000.

[40] K. R. Williams, K. Gupta, and M. Wasilik, "Etch Rates for Micromachining Processing—Part II", *J. MEMS*, Vol. 12, No. 6, December 2003.